

UNIVERSITY OF TARTU
Institute of Technology

Experiment Design for a 3D Ghost Imaging Setup Utilizing a LinoSPAD Sensor

MASTER'S THESIS IN ROBOTICS AND COMPUTER ENGINEERING

Author:
Jan BOGDANOV

Supervisor:
Andreas VALDMANN, PhD
Sergey OMELKOV, PhD



May 2019

TARTU ÜLIKOOL

Resüme

Tehnoloogiainstituut
Loodus- ja täppisteaduste valdkond

Tehnikateaduse magister

LinoSPAD maatrikstajuril põhineva kolmemõõtmelise arvutusliku kummituskuva teaduskatse kavand

Jan BOGDANOV

Automatiseerimise ja robotika suurenevad nõudmised seireseadmetele on tinginud kõrglahutusega kolmemõõtmelise kuva kiire arengu. Arvutuslikul kummituskuval põhinev kolmemõõtmeline (3D) kuva on arenev tehnoloogia, millel on harjumuspärase maatriksensoritepõhise 3D välkkuvaga (*flash imaging*) võrreldes suurem lahutusvõime. Paraku iseloomustab arvutusliku kummituskuva seadmeid tavaliselt kompromiss kujutise saamiseks kuluva aja ning saadava kujutise lahutusvõime vahel.

Magistritöös esitatakse LinoSPAD maatrikstajuril põhineva teaduseksperimenti kavand uude valguse lennuaja mõõtmisel põhineva 3D arvutusliku kummituskuva meetodi katsetamiseks. Vastupidiselt ühepikslilist valgusdetektorit rakendavale arvutuslikule kummituskuvale, kus üht pikslit kasutatakse terve stseeni pildistamiseks, jaotatakse esitatud meetodis tipptehnoloogilist prototüüp-maatrikstajuritit kasutades pildistatav stseen osadeks nii, et iga maatrikstajuri üksiku piksli vaateväli jälgib vaid osa stseenist. See lahendus lühendab märkimisväärselt kujutise saamiseks kuluvat mõõteaega, kuid ei vähenda saadava kujutise lahutusvõimet. Teaduskatse kavandi koostamisel analüüsiti nõudeid süsteemi valgusallikale ning ruumilisele valgusväljamodulaatorile ja uuriti LinoSPAD maatrikstajuri tööpõhimõtet. Lisaks täiendati kavandit footonihulgaarvutuste, haavelmüra ning üksikfootondetektori surnud aja simulatsioonidega ja esitatava süsteemikavandi ajastusahela katsetamisega.

Esitatud süsteemi ranged piirangud ajastamissignaalele nõuavad piisava sageduslahutuse saavutamiseks katse elluviimisel optimeerida ajastamissignaale vahendava elektroonika parameetreid. Sellegipoolest kinnitavad tehtud katsed ning simulatsioonid teaduseksperimenti kavandi rakendatavust uude 3D arvutusliku kummituskuva meetodi katsetamiseks.

CERCS: T111 pilditehnika; T120 süsteemitehnoloogia, arvutitehnoloogia; T121 signaalitöötlus; T181 kaugseire

Märksõnad: Kummituskuva, üksikpikslikuva, 3D kuva, SPAD-maatriks, GMAPD--maatriks, struktureeritud valgus, footonite lugemine

UNIVERSITY OF TARTU

Abstract

Faculty of Science and Technology
Institute of Technology

Master of Science in Engineering

Experiment Design for a 3D Ghost Imaging Setup Utilizing a LinoSPAD Sensor

by Jan BOGDANOV

High-resolution 3D-imaging is a rapidly developing field driven by the increasing sensing requirements of automation and robotics. Computational ghost imaging based 3D-imaging is an emerging technology, offering increased spatial resolution when compared to conventional 3D flash imaging systems. Usually, however, computational ghost imaging systems are characterized by their compromise between image acquisition times and image spatial resolution.

This thesis presents a LinoSPAD line sensor based experiment design for a novel time of flight based 3D computational ghost imaging method. Contrary to single-pixel computational ghost imaging, where a single-pixel detector is used for imaging the entire scene, the proposed method utilizes a state-of-the-art prototype sensor array to divide the scene to be imaged between the detector's individual pixels' fields of view. This approach significantly reduces the system's image acquisition times while avoiding a reduction in its spatial resolution. Prior to developing a final design, the requirements for the light source and the spatial light modulator and the capabilities of the LinoSPAD sensor were analyzed. Furthermore, the design was complemented with photon budget calculations, shot noise and detector dead time simulations, and preliminary setup tests focusing on the triggering scheme of the design.

The system's stringent timing requirements require the optimizing the parameters of triggering electronics in the experiment's implementation. Regardless, conducted tests and simulations confirm the feasibility of the experiment design for the novel 3D computational ghost imaging approach.

CERCS: T111 Imaging, image processing; T120 Systems engineering, computer technology; T121 Signal processing; T181 Remote sensing

Keywords: Ghost imaging, single-pixel imaging, 3D-imaging, SPAD-array, GMAPD-array, structured light, photon counting

Acknowledgements

Firstly, I thank my supervisor, Andreas Valdmann, for his outstanding supervision and for inspiring me with his knowledge and ideas. I also thank my co-supervisor, Sergey Omelkov, for his personal guidance, for sharing his spectacular insight of LinoSPAD and his support in conducting LinoSPAD tests.

Secondly, I thank Samuel Burri and Edoardo Charbon (EPFL) for providing the sensor and instructions for integrating it with the design.

Thirdly, I thank all the members of the Laboratory of Physical Optics for creating a truly enjoyable working environment and for their devotion to light sciences. Specifically, I thank Heli Lukner for encouraging me to consider progressing my studies. Also, I thank members Jürgen Luus, Joonas Ariva and Sandhra-Mirella Valdma, for our fruitful discussions and related work.

Fourthly, I thank Milrem Robotics for their support, innovative vision and knowledge-valuing attitude.

Fifthly, I thank my family for providing the necessary conditions and support throughout my studies and for understanding the importance of science and technology. Lastly, I thank Silja Veddel for her loving care and reinforcement.

Contents

Resümee	i
Abstract	ii
Acknowledgements	iii
Abbreviations and Acronyms	vi
Introduction	1
1 Theoretical Background	3
1.1 Overview of 3D-imaging Technologies	3
1.2 Development of Ghost Imaging	7
1.3 Ghost Imaging Pattern Design	9
1.4 Image Reconstruction	10
1.5 Suitability of Photodiodes in Ghost Imaging Applications	12
1.5.1 Geiger-Mode Avalanche Photodiodes	14
2 Experiment Design	19
2.1 Pattern Projection System	21
2.1.1 Selection Criteria for the Light Source	21
2.1.2 Fianium WhiteLase Supercontinuum Fiber Laser	22
2.1.3 Selection Criteria for the Spatial Light Modulator	22
2.1.4 Digital Micromirror Device DLP Lightcrafter™ 6500	23
2.2 LinoSPAD	24
2.2.1 LinoSPAD Firmware	25
2.2.2 Post-Processing	27
2.3 Simulations	28
2.3.1 Photon Calculations	28
2.3.2 Shot Noise Simulation	29
2.3.3 Detector Dead Time Simulation	29
2.4 System Setup	30
2.4.1 Setup Tests	32
Conclusion	37
Outlook	39

Bibliography	40
Appendix A – Shot Noise Simulation Results	44
Appendix B – Dead Time Simulation Results	49
Appendix C – Dead Time Induced Image Inversion	52
Non-exclusive licence to reproduce thesis and make thesis public	64

Abbreviations

2D	Two-dimensional
3D	Three-dimensional
CGI	Computational ghost imaging
DCR	Dark count rate
DMD	Digital micromirror device
FPA	Focal plane-array
FPGA	Field programmable gate array
FWHM	Full width at half maximum
GMAPD	Geiger-mode avalanche photodiode
GPIO	General purpose input output
IC	Integrated circuit
LiDAR	Light detection and ranging
LMAPD	Linear-mode avalanche photodiode
MCU	Microcontroller unit
MSE	Mean squared error
NIM	Nuclear Instrumentation Module
OPA	Optical phased array
PD	Photodiode
PDP	Photon detection probability
ROIC	Readout integrated circuit
SSI	Structural similarity index
TTL	Transistor-transistor logic
UART	Universal asynchronous receiver-transmitter
VCSEL	Vertical-cavity surface-emitting laser

Introduction

The methods of 3D-imaging – the process of acquiring a three-dimensional representation of an object or a scene – are steadily becoming more widespread as advances in detector, laser and computational technologies facilitate their development. The drive for this development is further fuelled by increasing demand for real-time 3D-imaging solutions – notably in the autonomous vehicles sector [1], where object detection and obstacle avoidance capabilities are essential. One emerging and prospective 3D-imaging technology is based on ghost imaging – an active sensing technique employing structured light to illuminate a scene and subsequently acquiring reflected light containing image data using a single-pixel detector [2]. However, using a single-pixel detector introduces intrinsic limitations to a ghost imaging based 3D-imager – as the desired spatial resolution of the image of the object increases, the time required to acquire this image also increases.

For practical imaging applications, a photodetector of sufficient sensitivity for sensing diffusely reflected light is mandatory. Technological progress in photodetector manufacturing and sensitivity has spearheaded the potential solution for advancing practical ghost imaging based 3D-imaging methods. Geiger-mode avalanche photodiode (GMAPD) arrays with the capacity to detect individual photons are rapidly evolving and their capabilities are sought in applications where detectable light levels are very low.

We propose a novel method which utilizes LinoSPAD – a GMAPD array with integrated timing circuitry – to acquire a 3D-image of a scene with significantly lower image acquisition times when compared to 3D ghost imaging setups using a single-pixel detector.

Aim of the Thesis

The main goal of this thesis is to develop a proof-of-principle novel design for the 3D computational ghost imaging (CGI) experiment with the LinoSPAD 256×1 array sensor as a core device in the setup. The design divides the scene to be imaged between the array sensor's pixel's, while still applying single-pixel CGI algorithm on each individual pixel. This approach significantly reduces the time required for acquiring an image, when compared to single-pixel 3D CGI. Furthermore, this method could render 3D CGI-based imagers a viable alternative to conventional 3D flash LiDAR based imaging techniques, as CGI can offer improved spatial resolution and detection range.

The full technical implementation of the experiment is a part of a larger project and the scope of this thesis encompasses the following critical elements of the experiment's design – structured light generation, optical component setup, analysis of LinoSPAD's capabilities and limitations, photon budget calculations and system integration with emphasis on

triggering. Additionally, simulations regarding the effects of shot noise and detector dead time are carried out. Lastly, preliminary tests concerning LinoSPAD, light generation and system triggering are conducted to provide additional insight into possible design specifications and component limitations.

Overview of the Thesis

This thesis is divided into two main chapters. The first chapter focuses on describing the primary theoretical aspects of ghost imaging. Firstly, comparative 3D-imaging technologies are briefly described. Subsequently, the chapter's sections give an overview of how ghost imaging has developed and its principle of operation. Furthermore, the pattern design and image reconstruction elements of the ghost imaging method are described. The first chapter concludes with an overview of essential photodetection devices with the emphasis on Geiger-mode avalanche photodiodes, as they are used in the proposed experiment setup.

The second chapter describes the proposed experiment's design. The chapter starts with the general overview of the experiment and its primary components – here the principal optical setup is proposed and the novel method is described. Followingly, the methods and devices for the generation and projection of structured light patterns is explained. There the focus is concentrated on the technical parameters of LinoSPAD and the selection criteria for the experiment's other instrumentation. Subsequently, the fundamental mechanisms of the LinoSPAD are explained which is followed by simulation methodology and results. The second main chapter ends with the description of the integrated system's setup. This section focuses mainly on triggering design, which is critical for acquiring correlated data from the experiment. The thesis closes with a conclusion and an outlook.

1 Theoretical Background

In this chapter, the theoretical aspects related to this thesis are described. Firstly, to provide a reference, an overview of various types of 3D-imaging technologies is given. Secondly, an introduction into ghost imaging is given, where the development of ghost imaging and its fundamental principles are described. Thirdly, critical knowledge concerning the creation of structured light using patterns is provided with a focus on creating patterns using the Hadamard basis. The central theory related to image reconstruction of ghost imaging is presented next. Subsequently, the appropriateness of various photodiodes in ghost imaging applications is discussed as measuring light intensities is one of the critical aspects in ghost imaging. As the detector used in the experiment prepared during this thesis employs highly sensitive Geiger-mode avalanche photodiodes, the last section focuses on describing this type of device.

1.1 Overview of 3D-imaging Technologies

The increasing interest in developing autonomous vehicles and advances in illumination and detection technologies have shifted the research focus of 3D-imaging sensor technologies toward longer range imaging systems, as depth information will have to be acquired from longer distances due to the relatively high speeds of the vehicles. Application scenarios of these automotive-oriented systems demand eye-safe radiation emissions, which create significant engineering challenges. Additionally, a large portion of the 3D-imaging systems on the market and in development strive to achieve image acquiring frequencies of at least 5 Hz [3–7]. Subsequently, an overview of the primary operation principles of various distance measurement and 3D-imaging technologies is given.

Distance Measurement Methods

One of the more common methods for using light to measure distances is the direct time of flight (ToF) method. Direct ToF-based systems operate by measuring the flight time of an emitted and subsequently detected pulse. As the speed of light in various conditions is known, the distance D between the system and the target object can easily be calculated as

$$D = \frac{\tau_R c}{2}, \quad (1.1)$$

where τ_R is the time elapsed from pulse emission to pulse detection and c is the speed of light. Particularly the requirement for increased range has boosted the development

of beam-steering based direct ToF (Figure 1.1) light detection and ranging (LiDAR) systems, which are characterized by high intensity peak pulses that can more easily be made to comply with the set guidelines of the laser eye safety standard IEC 60825 [8].

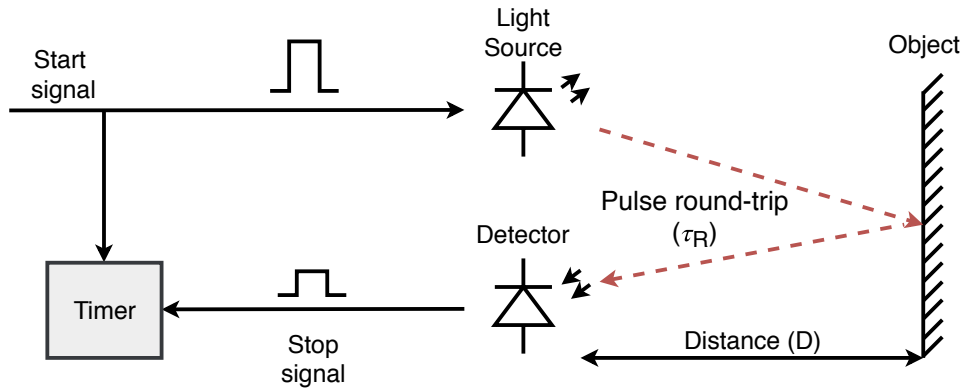


FIGURE 1.1: Direct ToF detection utilizes a high-speed electronic timer which is initiated simultaneously with a narrow pulse width high-peak light pulse emission. The timer stops when a signal of sufficient intensity is detected. This method is also called time-domain reflectometry-based distance measurement [8].

Another technique employing light in distance sensing applications is the indirect ToF method. In continuous-wave radar technology, heterodyning is a known method and has been used extensively [9]. Similar principles for range-finding can be applied in light-based 3D-imaging systems (Figure 1.2). This indirect ToF method may allow for simultaneous Doppler based velocity measurements and also decrease detector complexity [10]. Furthermore, in a heterodyne detection receiver, the signal-to-noise ratio corresponds to the amount of photons incident, while a direct ToF receiver requires a signal with intensities high enough that its shot noise overshadows other noise sources [11]. With heterodyne receivers, it is easier to achieve sub-millimeter range resolution systems over very short distances, making it suitable for surface imaging applications as an example [12]. Achieving a comparable range resolution in a direct ToF system would require a sub-picosecond pulse-width laser, which can currently be considered economically unfeasible in most consumer applications.

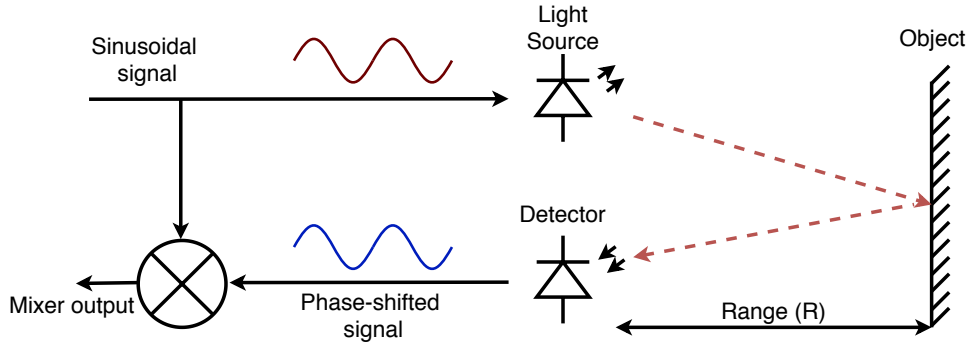


FIGURE 1.2: In indirect ToF detection a continuous sinusoidal wave with varying frequency is emitted towards an object and also relayed to a frequency mixer. The phase shifted signal is detected and relayed to the mixer’s second input. The mixer outputs a two-frequency signal containing the sum and the difference of the two frequencies and the higher frequency is discarded. The resulting lower frequency is directly correlated to the distance (R) between the system and the target object. The method can be implemented with signals modulated at radio frequencies and with signals at optical frequencies. This method is also called frequency-domain reflectometry-based distance measurement [13].

Beam Steering-Based 3D-Imaging

Due to the many practical applications of 3D-imaging, various methods are being studied and have been developed for capturing a 3D representation of an object (Figure 1.3). Beam steering based 3D-imagers usually direct one or more laser beams to a point in space, get the distance to the closest object in that direction and rapidly repeat the process. Currently, the technologically most mature and market-ready technology for beam steering implements electromechanical solutions such as electric motors [14, 15]. However, due to the relatively high inertia of moving elements in these systems, micromirror-based beam steering is seen as an alternative and is being rapidly developed for consumer markets [16–18]. Alternatively, a 3D-imager without any moving parts – a solid-state imager – could potentially increase the robustness and longevity of these devices and reduce the production costs at sufficiently high volumes [19]. Thus, another emerging solution is the dispersion-based beam steering, which employs tunable-wavelength lasers and dispersive elements, such as diffraction gratings or prisms in order to achieve beam steering [20]. Furthermore, optical phased-array-based (OPA) beam steering offers another potential method for solid-state beam steering, although it can be realized as true solid-state method, OPA-based beam steering can also be implemented with micromirror-technology [17]. An OPA uses the equivalent of many individual phase-shifters, which gradually alter the phase at adjacent points of an incident undisturbed wavefront [10, 21]. Resulting constructive interference directs the light beam in the desired direction while destructively interfering with the light waves propagating in the undesired direction [21].

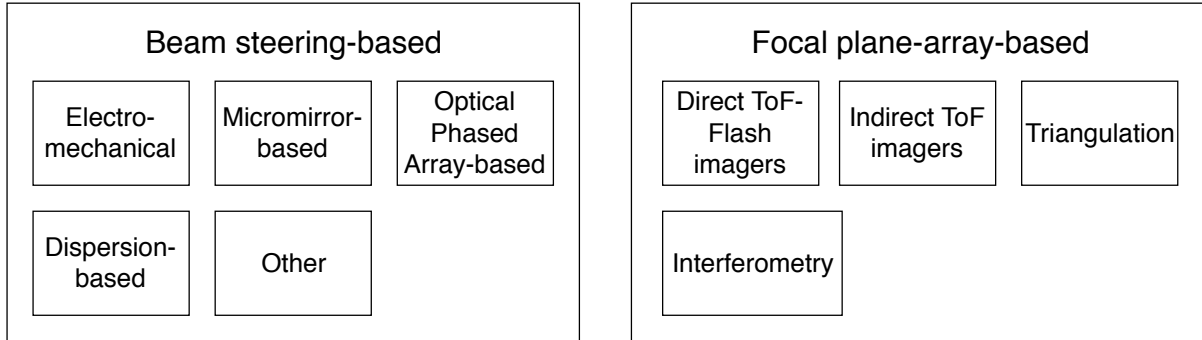


FIGURE 1.3: Although there are many methods for 3D-imaging that are being developed simultaneously, there are methods, which are not in active development. For example, beam steering-based solutions such as volume holographic step steering, birefringent prim-based beam steering, liquid crystal polarization grating-based beam steering or electrowetting-based beam steering are currently, due to manufacturing complexity or inherent technological limitations, not being actively researched [21].

Focal Plane Array Based 3D-Imaging

Focal plane array (FPA) based 3D imagers usually employ light sources and cameras for 3D image acquisition. Flash 3D-imagers use a light source to illuminate a scene of interest and employ an array of detectors to capture the reflected light from the scene in one measurement (Figure 1.4). This method has the advantage of not requiring beam steering, thus reducing the stabilization precision requirements and possibly size and weight requirements. Since the amount of energy returning to the receiver is relatively small and it is incident on a relatively large detector array area, a high peak-illumination power and/or high sensitivity detectors are required [11]. Triangulation based structured illumination 3D-imaging techniques may employ a projector for illuminating an object with structured patterns while observing the object with a camera. Through the use of complex image analysis algorithms a 3D image can be obtained [22]. Interferometry uses the phase of the optical wave to acquire accurate depth information. In practice, however, both triangulation- and interferometry-based methods can only be implemented to relatively short distances [23].

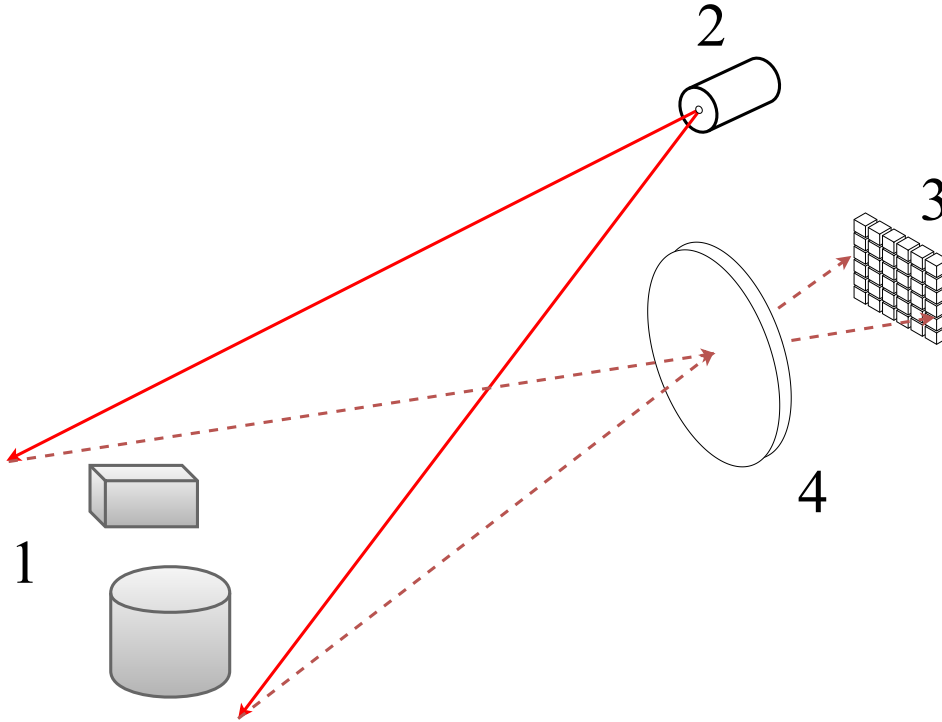


FIGURE 1.4: A direct ToF (Figure 1.1) 3D flash imager example where an area of interest (1) is illuminated using a pulsed laser (2). The diffusely reflected light is focused by a lens (4) to an FPA (3) which itself is synchronized to the laser. The laser pulse provides a reference time against which each of the detector's pixels is capable of determining when the reflected light reached the pixel. An indirect ToF 3D flash imager (Figure 1.2) can also be implemented in a similar manner [11].

1.2 Development of Ghost Imaging

Ghost imaging is generally known as an imaging method, which employs light that has not interacted with a scene or object that is the target of imaging [24]. Ghost imaging was initially interpreted as a quantum entanglement phenomenon occurring due to the entanglement of source photons using a bi-photon light source. A transmissive 2D amplitude mask object facing an immovable single-pixel detector is illuminated with signal photons while a scanning detector or a detector with high spatial resolution observes the cross section of the reference beam at specific distances resulting in an intensity pattern. With this method an image of a target was acquired from the coincidence counting rate of the two beams [25].

Contrary to the assumption that ghost imaging is solely a quantum phenomenon-based technique, experiments with pseudo-thermal light sources have proved that ghost imaging can be described using classical electromagnetics. Due to this, in order to reconstruct the image of the object, the entanglement of photons is not required (Figure 1.5) [24, 26].

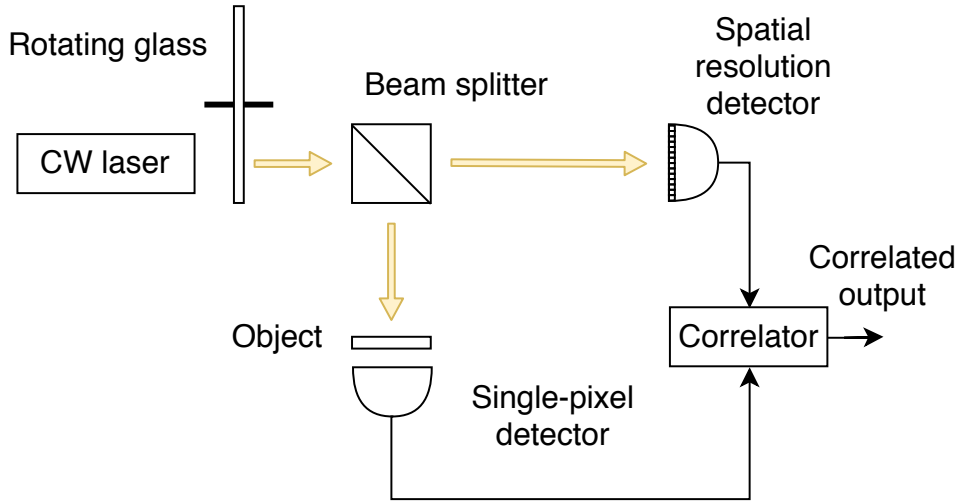


FIGURE 1.5: In ghost imaging with a pseudo-thermal light source, a ground rotating glass illuminated with a continuous-wave (CW) laser produces time-dependent speckle pattern through stochastic interference. Light is divided and guided onto a reference detector with high spatial resolution and a single-pixel object detector. From the correlation of intensity fluctuations a reconstructed image of the target object is produced [26].

In 2008 [27] it was shown that ghost imaging is realizable using only a single pixel detector (Figure 1.6). This was achieved using a continuous-wave laser-generated beam incident on a spatial light modulator (SLM), which deterministically modulated the phase beam to illuminate the object with varying light patterns. Knowledge of the deterministic modulation of the beam enabled the use of diffraction theory to compute the intensity pattern that otherwise had to be acquired using a reference detector. Furthermore, this method allows the subtraction of time average from the acquired intensity pattern, resulting in a computational ghost image without background noise [27]. In addition, discarding the detector with spatial resolution has the benefit of ignoring the inherent sub-one quantum efficiency value of array detectors, which deteriorates the signal-to-noise ratio of the pattern measurement. Thus, the computational ghost imaging will persistently surpass classical ghost imaging using a second detector with spatial resolution when comparing image reconstruction quality [28].

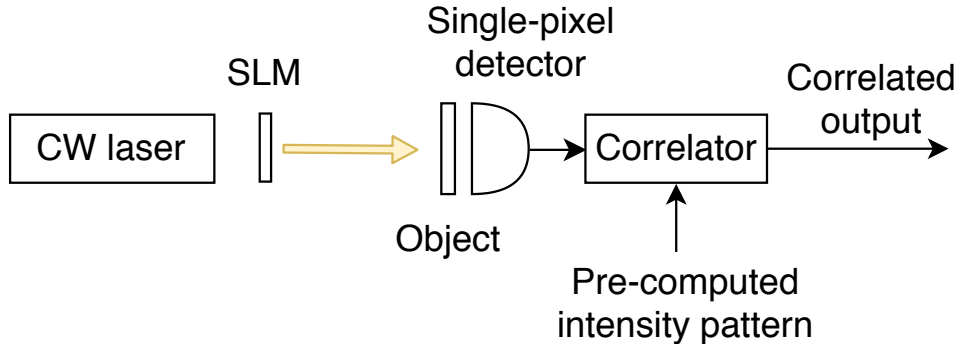


FIGURE 1.6: In computational ghost imaging, light is modulated with known patterns and later used to pre-compute the intensity patterns that otherwise would have to be acquired using a high spatial resolution detector [27].

Instead of using a phase-modulating SLM an amplitude-modulating SLM can also be used allowing the projection other types of patterns, besides diffraction patterns. This is beneficial, as the amplitude-modulated SLM patterns do not have to be pre-computed and can be used as is, thus lightening the computational complexity of the process. An example of a computational ghost imaging configuration (Figure 1.7) consists of a projector and an SLM and its conditioning lens that can be used to project patterns onto a target object [29].

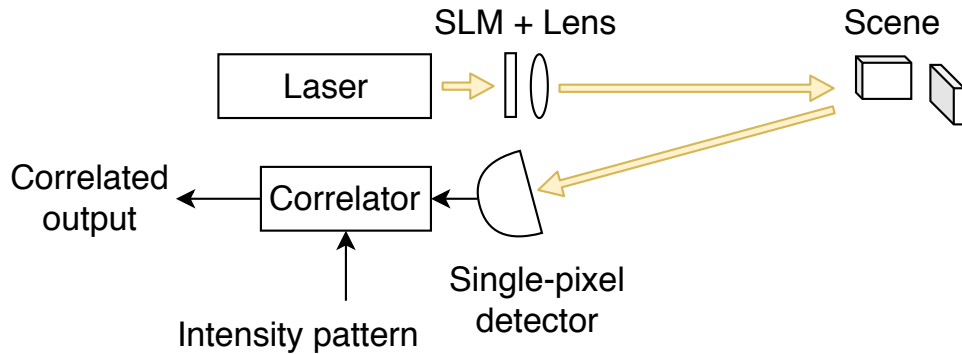


FIGURE 1.7: A computational ghost imaging setup in a bi-static configuration using amplitude-modulating SLM can be used for imaging a scene. The reflected light's intensity is similarly measured by a single-pixel detector [29].

1.3 Ghost Imaging Pattern Design

When conducting ghost imaging, the nature of the patterns projected onto a target object has significant impact on the imaging process. It is possible to create random patterns for ghost imaging applications. However, it has been shown that randomly generated patterns have inherently overlapping spatial information between patterns, ultimately resulting in

reduced image reconstruction quality. In order to reconstruct an image of sufficient quality using random patterns, the number of random patterns M should be significantly greater than the resolution of individual pattern N . Thus, the reconstruction of an object using 256×256 patterns would require the object to be sampled with $\gg 256^2$ patterns, which imposes significant limits to potential practical applications of ghost imaging [28].

Additionally, orthogonal patterns can be used in ghost imaging. In contrast to random patterns, orthogonal patterns are void of any spatial overlapping and this increases the contribution of every individual pattern. A known method for creating orthogonal patterns is provided by the Hadamard basis and it has been used previously in ghost imaging experiments [28, 30]. The primitive of a 2×2 Hadamard matrix is

$$H_2 = \begin{bmatrix} 1 & 1 \\ 1 & -1 \end{bmatrix}. \quad (1.2)$$

A Hadamard matrix exists for every matrix of order 2^k and is expressed as

$$H_{2^k} = \begin{bmatrix} H_{2^{k-1}} & H_{2^{k-1}} \\ H_{2^{k-1}} & -H_{2^{k-1}} \end{bmatrix}. \quad (1.3)$$

Using this method any 2^k order square Hadamard matrix can be generated using the Kronecker product $H_2 \otimes H_2^{k-1}$ and each pattern illuminating the target object conforms to one row of the large matrix, which can be shaped into suitable forms for projecting. The usage of orthogonal patterns ideally enables the reconstruction of an N pixel image with N measurements [28]. If there was any prior knowledge of the object, it would be possible to design the creation of encoding patterns in a way which is optimized for a specific target. However, in most cases prior knowledge of the objects is not available and the encoded patterns have to be designed to offer as much information as possible per projection [28]. It is possible to use compressive schemes for structured illumination where patterns with the most significant intensities measured in the previous frame are selected for illuminating the object. This potentially enables quicker image acquisition and may be suitable in real-time applications of imaging. Furthermore, careful pattern design may yield additional benefits – for example, by displaying a pattern and subsequently its inverse pattern onto an object, differential measurements are taken which can be used to eliminate certain causes of noise, such as variations in background light intensities [31].

1.4 Image Reconstruction

In computational ghost imaging (Figure 1.6), the randomly generated or pre-generated and known patterns projected onto an object are effectively used to evaluate the correlation of their spatial frequencies with the object. The result of this evaluation from each pattern is acquired using the single-pixel photodetector and this result becomes the

weight of how well a pattern matched the target object. As each known pattern now has a weight attached to it, both data can be used to reconstruct (Figure 1.8) the image of the object as

$$I_r = \sum_{i=1}^N (S_i - S_m) P_i, \quad (1.4)$$

where I_r , is the reconstructed image, S_i is the signal intensity associated with its corresponding pattern P_i and S_m is the average value of the signals S_i [28].

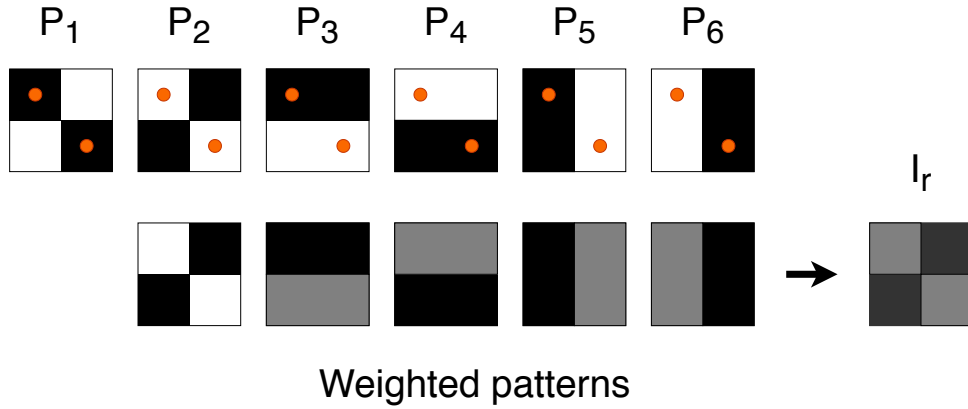


FIGURE 1.8: A visualization of a 2×2 image reconstruction process. Patterns $P_1 - P_6$ illuminate two objects represented by orange dots. Patterns 2-6 produce weighted patterns and as no signal returns from the first pattern, the resulting weighted pattern is zero. The summation of the weighted patterns produces the reconstructed image I_r [28].

3D-Image Reconstruction

Computational ghost imaging can be used to acquire 3D-images. By using a pulsed light source, a fast photodetector and timing circuitry, depth information from a scene can be acquired by implementing the time of flight principle (Figure 1.1). In comparison to the 2D computational ghost imaging configuration (Figure 1.7), temporal behaviour of light pulses reflected from the scene become relevant. As the objects in the scene to be imaged are located at different distances, the light reflected from the objects is temporally broadened (Figure 1.9). Contrary to 2D computational ghost imaging, where the signal intensities for each pattern are integrated, 3D computational ghost imaging algorithm uses M sampled intensity values from a measured light signal to subsequently reconstruct M 2D images. This results in a time-varying array of 2D images. Transverse pixels (x, y) in the array also have a series of intensity values along the longitudinal axis (z) , which are correlated to the temporal structure of the detected light pulse and the reflectivity of the object to be imaged. Depth information is constructed by interpolating

each pixel's temporal signal and finding its maximum. Furthermore, by averaging pixels of the time-varying array 2D images along its longitudinal axis, reflectivity values of the object can be acquired [31].

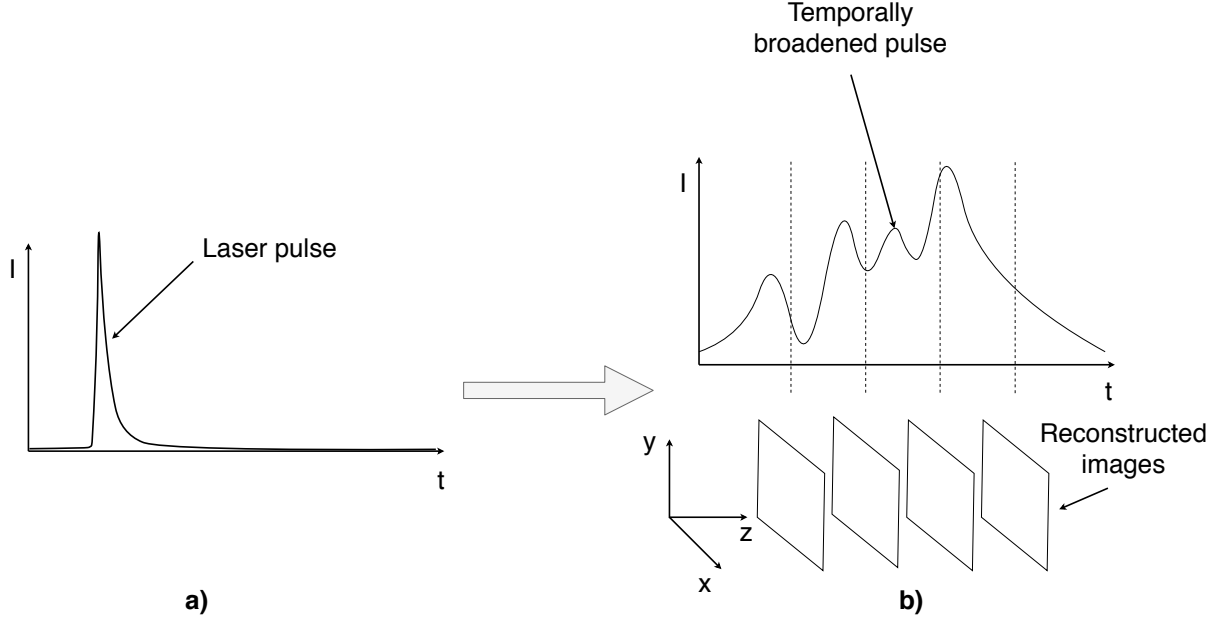


FIGURE 1.9: **a)** A pattern encoded laser pulse is projected onto a target object and diffusely reflected. **b)** Temporally broadened signal is acquired and discretized. Subsequently, for each acquired laser pulse, discretized light intensity values are paired with their respective patterns and a series of images is reconstructed [31].

1.5 Suitability of Photodiodes in Ghost Imaging Applications

Various types of photodiodes are suitable for use as bucket (single-pixel) detectors in ghost imaging experiments. PIN-type photodiodes (PD's), linear-mode avalanche photodiodes (LAPDs) and geiger-mode avalanche photodiodes (GMAPDs) have suitable parameters, but so far only PDs have been successfully used in ghost imaging experiments as imaging range has not been the focus of these experiments [31]. PDs are photodetectors that are based on reverse-biased (photoconductive) or zero-biased (photovoltaic) p-n junction. A photon with sufficient energy incident on the p-n junction will generate an electron-hole (e-h) pair with the probability of $\eta_{quantum}$, which is the quantum efficiency of the PD. A generated e-h pair will result in one charge carrier e generated in the PD's external circuit. Thus a photocurrent i is generated and expressed as

$$i(t) = \frac{\eta_{quantum}e}{hf_0}P(t), \quad (1.5)$$

where h is the Planck's constant, f_0 is the optical frequency of the incident photon and P is the optical power incident on the p-n junction [32].

Another type of photodiode is the linear-mode avalanche photodiode (LAPD), which fundamentally follows the same principles as PIN-type PDs, but differ from PIN PDs by operating at higher reverse-bias voltages. This results in higher electric fields across the p-n junction, effectively creating an avalanche zone. A photon with sufficient energy incident on the avalanche zone will create a e-h pair, which in turn will generate a charge eM_0 in the LAPD's external circuit, where M_0 is the avalanche gain of the LAPD. Thus the photocurrent i_{APD} of the LAPD is

$$i_{LAPD}(t) = M_0 i_p(t), \quad (1.6)$$

where i_p is the photocurrent generated from primary e-h pairs (Equation 1.5). The avalanche gain property occurs in LAPDs due to impact ionization – the capability of photon-generated e-h pairs to generate secondary e-h pairs. The avalanche mechanism of an LAPD is self-limiting and ends when all the primary and secondary electrons have left the avalanche zone [32]. A comparison of a silicon-based PIN PD's and LAPD's typical parameters is shown in table 1.1. Compared to an LAPD, a PIN-type PD has relatively low sensitivity and thus is usually unsuitable for reflectometry-based distance measurement (Section 1.1) applications. LAPDs incorporate significant inherent gain, but require more complex electrical circuitry for satisfying required voltage biasing conditions and still use analog signal conditioning front-end circuitry. There also exists LAPD-based array sensors, which may require complex read-out integrated circuits (ROIC) for capturing and storing image data. These factors make the LAPD viable for short-range reflectometry-based distance measurement applications, but for long-range imaging additional sensitivity is needed [11]. Certain LAPD's also exhibit gain factors high enough to sense single photons, however such detectors currently need require to be cooled to approximately 100 K temperatures [33].

TABLE 1.1: Typical parameters of silicon-based PIN-type PDs and LAPDs [34, 35]

Parameter	PIN	LAPD
Wavelength range (nm)	400-1100	400-1100
Responsivity (A/W)	0.6	77-130
Quantum efficiency (%)	65-90	77
Gain	1	150-250
Bias voltage (V)	10-100	>220
Dark current (nA)	1-10	0.1-1.0
Capacitance (pF)	1.2-3	1.3-2
Rise time (ns)	0.5-1	0.1-2

1.5.1 Geiger-Mode Avalanche Photodiodes

Geiger-mode avalanche photodiodes (GMAPDs) or alternatively single-photon avalanche diodes (SPADs) are semiconductor photodetectors utilizing a p-n junction that is reverse biased above its breakdown voltage V_{br} , where V_{br} is defined as the reverse bias voltage of a p-n junction of a diode above which there is an exponential increase in the leakage current of the device. The resulting electric field across the p-n junction creates conditions where a photon incident on it initiates a self-sustaining charge carrier avalanche due to the impact ionization of the charge carriers created. The resulting current-spike does not require any additional amplification for successful detection. Since the avalanche is self-sustaining, the process will have to be disrupted (quenched) externally in order to prevent damage to the GMAPD. (Figure 1.10) [32, 36].

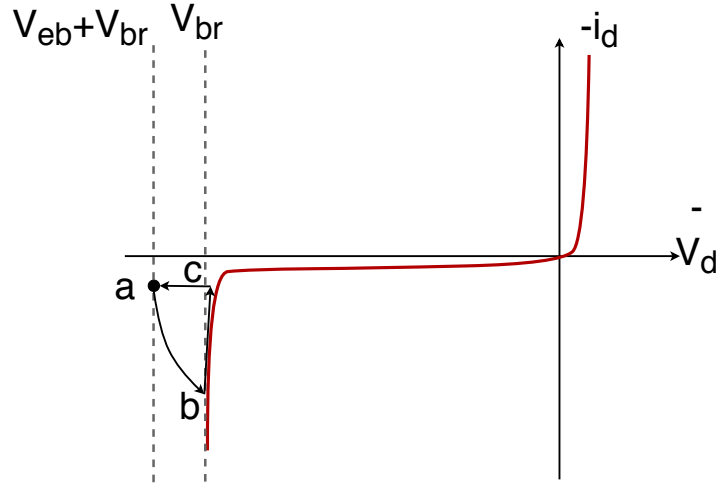


FIGURE 1.10: GMAPD current-voltage curve of a GMAPD with a breakdown voltage of V_{br} , excess bias voltage of V_{eb} , voltage across the GMAPD V_d and GMAPD current i_d . **a)** An incident photon triggers a self-sustaining avalanche. **b)** Front-end electrical circuit decreases V_d below V_{br} and thus quenches the avalanche. **c)** Front-end electrical circuit restores the V_d to V_{eb} above V_{br} and thus the GMAPD is ready to detect another photon [32].

Ideally, the self-sustaining avalanche can only be initiated by an incident photon. In practice, injection of a charge carrier into the depletion region of a GMAPD by thermal generation, trap-assisted generation or tunneling can also trigger an avalanche. Avalanche events not related to incident photons are expressed as the dark count rate (DCR) n_{DCR} and they are identical to events photonic events. The amount of dark counts N_{DCR} during a measurement duration of t_{meas} can be expressed as

$$N_{DCR} = n_{DCR}t_{meas}[32]. \quad (1.7)$$

The DCR also determines a GMAPD's noise and dynamic range. Due to no external amplifiers, only dark count events and shot noise can be considered as noise sources in a GMAPD-system. The standard deviation of the measured Poisson-distributed dark count events is shown as

$$\sigma_{N_{DCR}} = \sqrt{n_{DCR} t_{meas}}, \quad (1.8)$$

which sets the minimum noise of a GMAPD system in no-light conditions. The dynamic range DR of a GMAPD system is

$$DR = 20 \log \left(\frac{n_{max}}{\sqrt{n_{DCR}}} \cdot \sqrt{t_{meas}} \right), \quad (1.9)$$

where n_{max} is the maximum count rate. Averaging diminishes the relative impact of the GMAPD's noise and therefore the dynamic range of a GMAPD system is proportionate to the $\sqrt{t_{meas}}$ [32].

Whenever an avalanche is triggered the process of detection avalanche, avalanche quenching and recharging of GMAPD voltage V_d to excess bias voltage V_{eb} occurs. The time required for the GMAPD to be able to detect the next incident photon after a detection event is expressed as the dead time t_{dead} . Two types of quenching circuits can be distinguished – passive and active circuits. In its most straightforward form, passive quenching (Figure 1.11) is realized with a resistor in series with a GMAPD. A photon incident on a GMAPD initiates a self-sustaining avalanche. As the avalanche current increases the voltage drop on the resistor in series with the GMAPD also increases. This continues until V_{GMAPD} decreases to below the GMAPD's breakdown voltage V_{br} and the avalanche ceases to be self-sustaining, thus eventually stopping. Afterwards, the V_{GMAPD} is raised to V_{eb} via resistor R_Q and the circuit is ready to detect another photon [32].

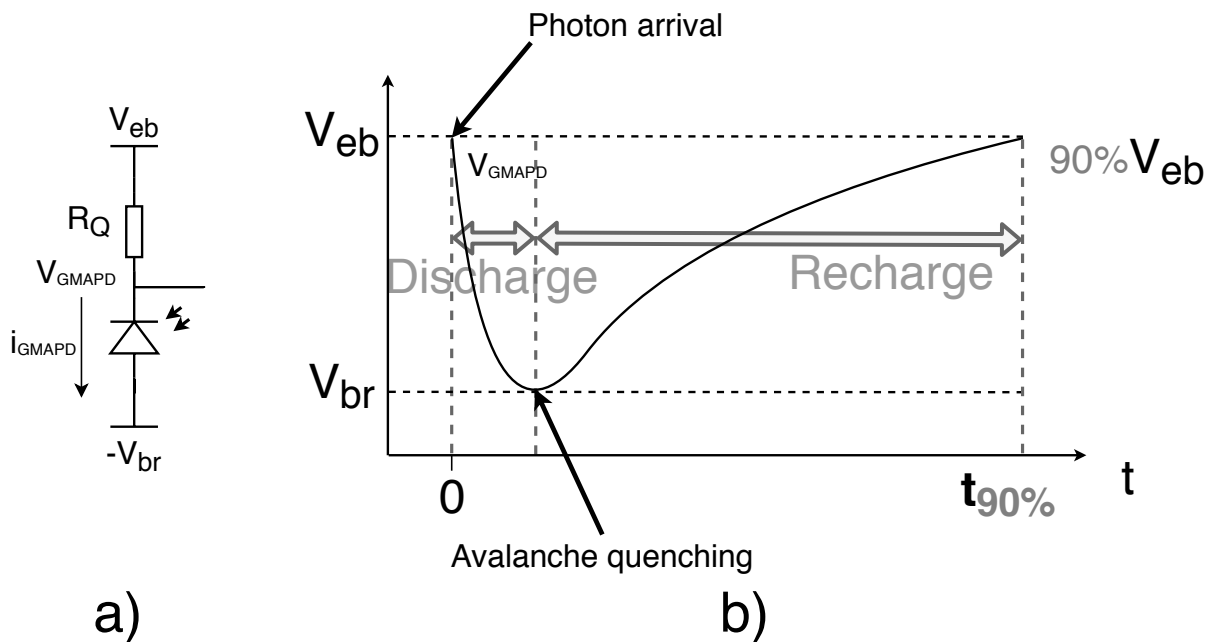


FIGURE 1.11: **a)** A passively quenched negative-drive GMAPD circuit realized with with series resistor R_Q . With V_{eb} as the excess bias voltage, V_{GMAPD} as the GMAPD floating voltage, V_{br} as the GMAPDs breakdown voltage and i_{GMAPD} as the GMAPD current. **b)** $t_{90\%}$ is the time where the V_{GMAPD} has reached 90% of V_{eb} [32].

A more refined GMAPD front-end architecture (Figure 1.12) is often required in practical applications. In a passively quenched circuit, a resistor can be realized with a MOS transistor. This enables the dynamic control of the quenching resistance and thus some control over dead time duration. Furthermore, an inverter connected to the floating node of the GMAPD is often used to create a digital output pulse [32].

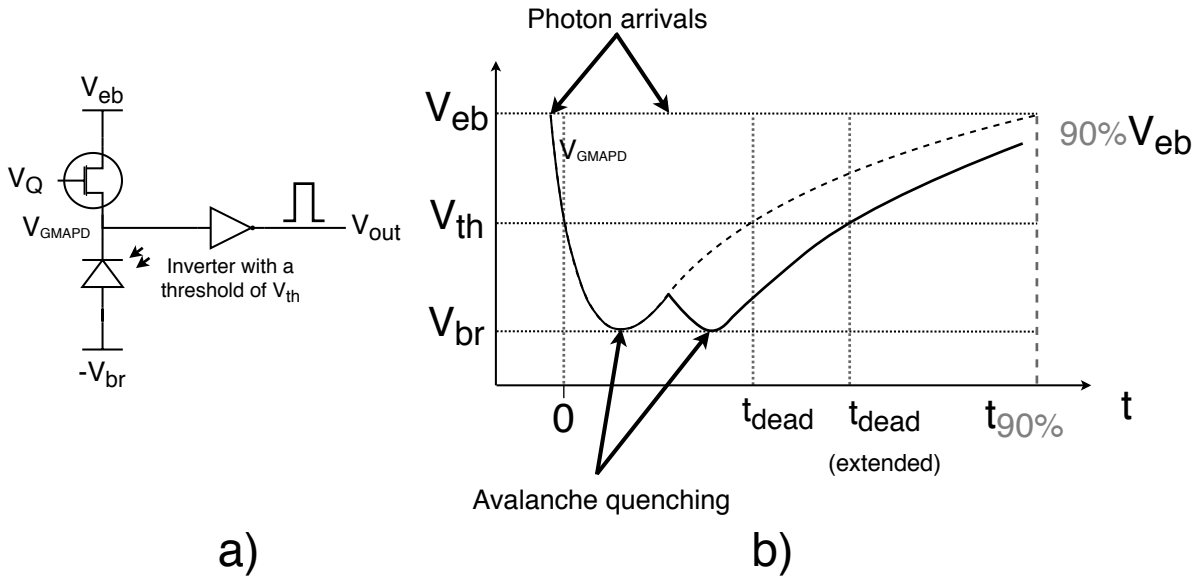


FIGURE 1.12: **a)** A passively quenched negative-drive GMAPD circuit, where V_Q is used to control the quenching resistance and an inverter sets the threshold V_{th} for creating digital output pulses. **b)** The occurrence of two subsequent short-interval photon arrivals in a passively quenched GMAPD system extends the dead time of the GMAPD without detecting the second arrival. This extension of the dead time or detector paralysis can transpire as long as $V_{GMAPD} > V_{br}$, because the condition for avalanche breakdown is satisfied [32].

In order to prevent detector paralysis, active quenching front-end circuitry can be used (Figure 1.13). After photon arrival, V_Q is used to pull the floating node of the GMAPD to ground. The GMAPD is rapidly discharged and V_{GMAPD} is held at 0 volts for a period of time to reduce afterpulsing – a secondary avalanche breakdown caused by the entrapment and the subsequent release of charge carriers due to lattice defects in the p-n junction. Followingly, V_Q is opened and V_R is closed, which rapidly raises the V_{GMAPD} to V_{eb} , after which, the V_R is opened and the system is ready to detect another photon [32].

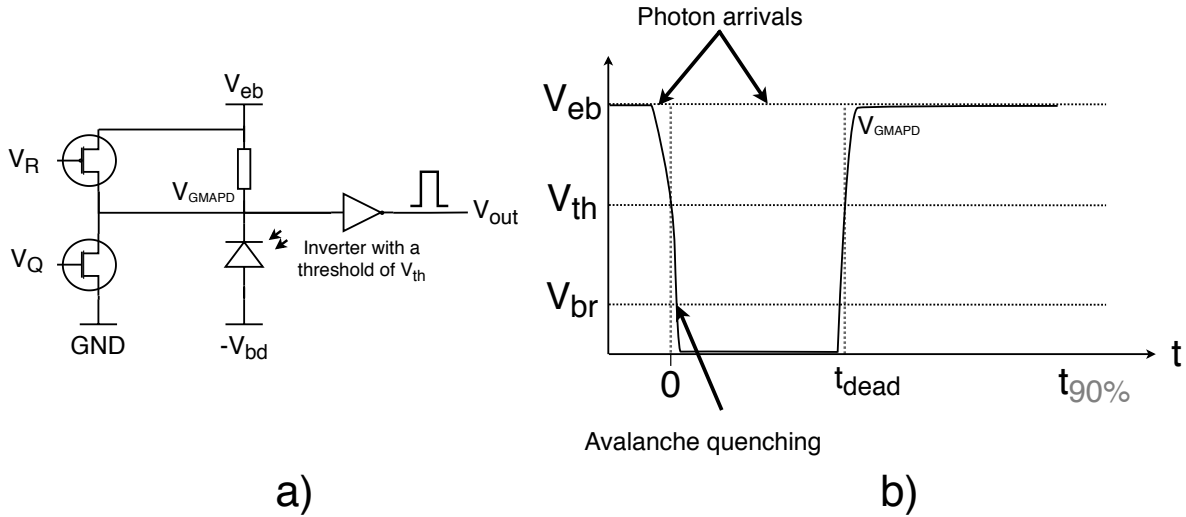


FIGURE 1.13: **a)** An actively quenched negative-drive GMAPD circuit has the benefits of reduced afterpulsing, fast recharge and non-extendable dead time at the cost of increased area requirements on the integrated circuit and increased optical stack, which may reduce photon detection efficiency. **b)** An actively quenched GMAPD front-end is not subjectable to detector paralysis due to V_{GMAPD} being held below V_{br} after photon detection [32].

As GMAPD's are very sensitive, their imagers have the advantage of requiring low pulse energy high repetition rate lasers and they can also be used to for passive imaging in the near-infrared spectrum. Furthermore, in practical high-end applications they can be sufficiently cooled using thermoelectric cooling. The disadvantage of GMAPD-based 3D imagers is that they require multiple return pulses from the object, while the LMAPD-based imagers are capable of obtaining a scene in one return. Also, the photon detection probability (PDP) of GMAPD's has to be kept relatively low (typically 10-20%), due to the bias of detecting objects that are closer to the detector, which is caused by the dead time of the detector. The photons diffusely reflected from an object closer to the detector are more likely to reach the detector sooner than the photons reflected from more distant objects. Thus, with a high PDP GMAPD-based 3D-imager, a significant proportion of photons reflected from more distant objects would arrive at the detector during its dead time [33].

2 Experiment Design

As single-pixel computational ghost imaging (CGI) systems exhibit considerably high image acquisition times, a direct time of flight based 3D computational ghost imaging system using the LinoSPAD line array sensor is proposed (Figure 2.1). By dividing the scene to be imaged between the line sensor’s individual detectors and applying CGI algorithms to each individual pixel of the detector, substantial decrease in image acquisition times can be achieved. Notably, this approach is novel and enabled by the cutting edge prototype sensor LinoSPAD.

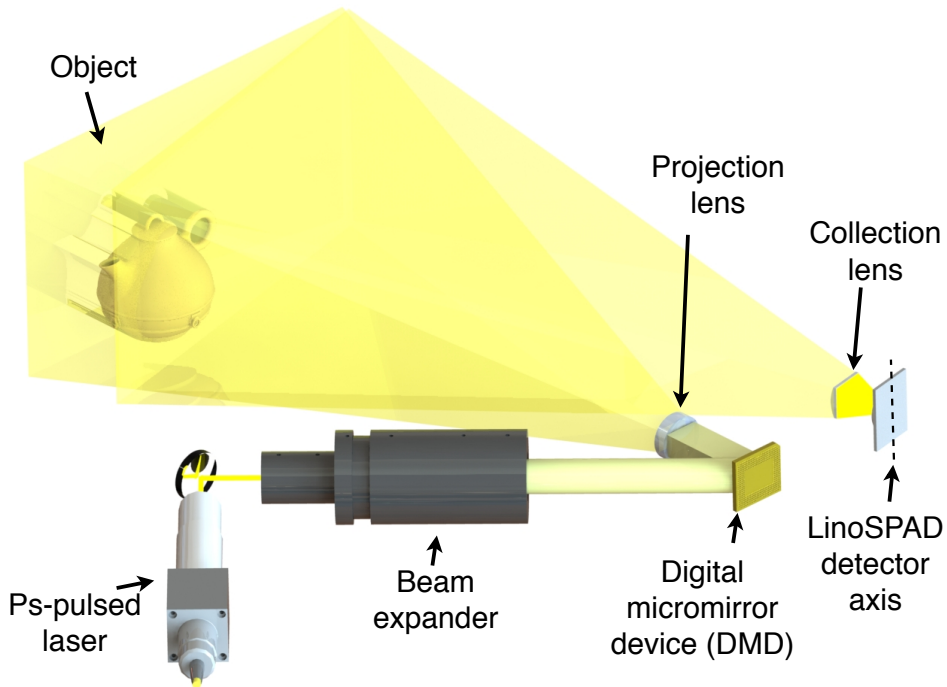


FIGURE 2.1: A 3D CGI experiment setup, where a picosecond pulsed laser’s output beam is guided onto a digital micromirror device, which forms a sequence of patterns projected onto a target object to be imaged. The light diffusely reflected from the object is collected and projected onto a LinoSPAD line sensor.

Although 3D computational ghost imaging has been successfully demonstrated before with a single pixel PIN-type photodiode [31], using a GMAPD array enables applying techniques that offset some of the inherent application challenges of computational ghost imaging – notably the time required to acquire a single image. It is possible to reduce the

number of orthogonal patterns necessary for obtaining an image by a factor equal to the number of elements in the GMAPD array (Figure 2.2). Thus, obtaining a 256×256 image of a target object with a 256×1 GMAPD array would require projecting only 256 patterns or 512 patterns, when respective inverse patterns are used for reducing background noise.

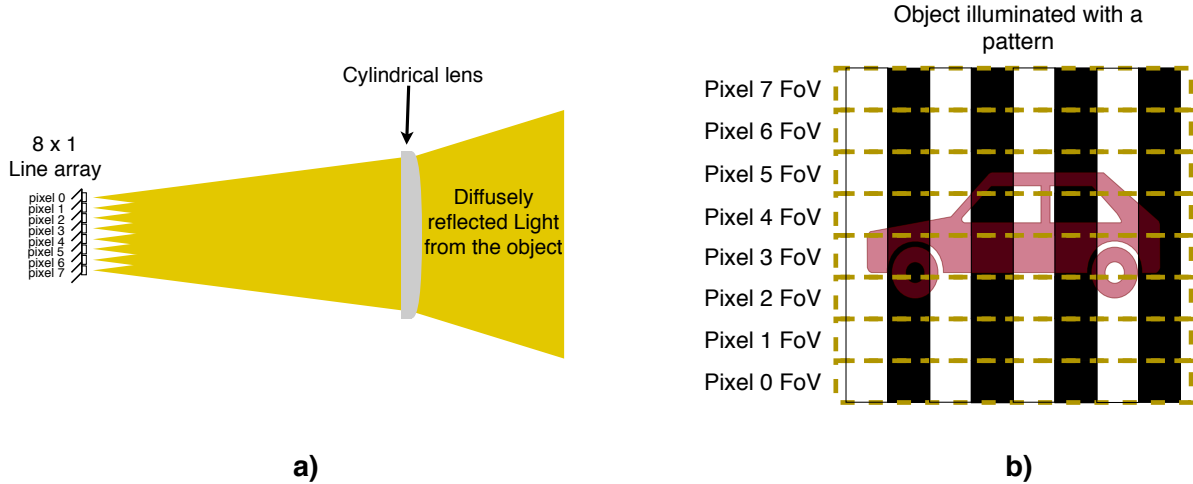


FIGURE 2.2: **a)** Light back-scattered from an object is gathered by a cylindrical lens and guided onto a line sensor (8×1 in this example). **b)** The field-of-view (FoV) for each individual pixel is divided so that their combined FoV's cover the desired total field of view. Thus, in this example, each pixel effectively views $\frac{1}{8}$ th of the area to be imaged. The computational ghost imaging algorithm can be applied to each pixel separately and the resulting reconstructed images are combined into a final image in a significantly lower time span when compared to using just a single-pixel detector.

Acquiring a 3D-image in the proposed design uses the method described in chapter 1.4. As the design utilizes a GMAPD-based detector, the temporal shape of the diffusely reflected signal will have to be acquired over a series of measurements. This is due to each of the LinoSPAD's pixels being able to detect, on average, a single photon from a single pulse emitted by the laser. During the series of measurements the arrival times of detected photons are placed into time-bins and recorded in a histogram, recording the temporal shape of the light pulse for each pattern and for each LinoSPAD pixel.

In this chapter, the experiment and its parts are outlined. An overview regarding the principal components – NKT Photonics Fianium WhiteLase High Power Supercontinuum Fiber Laser, LinoSPAD sensor and the Texas Instruments Digital Micromirror Device DLP LightcrafterTM 6500 – used in the experiment and their application aspects is given. Furthermore, simulations conducted during the thesis are characterized. Lastly, the experiment setup, its control software and the performed preliminary setup tests are described.

2.1 Pattern Projection System

For a 2D computational ghost imaging application, a commercially available video projector would likely be suitable. However, a 3D ghost imaging application requires a projector that is capable of switching patterns at high frequencies and at very short light pulse durations. Thus, for the purposes of this experiment, a projector with a specialized light source is required. A projector used in the experiment's design producing orthogonal patterns demands a light source and a controllable device capable of modulating light – a spatial light modulator. Furthermore, electrical interfaces facilitating trigger signals are required.

In this chapter, an overview of the primary criteria and limitations for pattern projection components of the proposed setup is given. Furthermore, the primary parameters and principles of operation of the components selected satisfying the set criteria are outlined.

2.1.1 Selection Criteria for the Light Source

In the proposed experiment, a pulsed light source's pulse emission has to be controllable or at least the light source will have to provide a reference signal indicating the emission of a light pulse. Furthermore, the light source sets constraints for the theoretical maximum range of detection d_r , expressed as

$$d_r = \frac{ct_l}{2}, \quad (2.1)$$

where c is the speed of light and t_l is the light source's repetition period. This condition additionally impediments the proposed experiment as it is using a photon-counting detector. As the system requires hundreds to thousands of measurements to acquire an image, a light source with a higher repetition rate accelerates that process, but coincidentally limits the system's maximum detection range. For the purposes of the proposed experiment, a maximum detection range of 10 metres is set. In addition, the light source's pulse width limits the maximum depth resolution r_d of the system, calculated as

$$r_d = \frac{ct_p}{2}, \quad (2.2)$$

where c is the speed of light and t_p is a light source's pulse width. This condition requires that a picosecond-range pulse-width light source is used – e.g. photons detected from a 1 ns pulse-width light source introduce a ~ 15 cm uncertainty to the measured distance.

In the proposed experiment, the light source's output power has to be sufficient for exceeding the shot noise limitation of the detector at distances of up to 10 metres at a field of view of 10 degrees, which is set by LinoSPAD's and it's focusing lens parameters. In a practical application, a system's light source would ideally be at near-infrared

wavelengths, as it is invisible to the human eye. However, in the proposed experiment, visible wavelengths would simplify setting up the experiment. Lastly, the light source’s availability in terms of its cost has to be considered. Light sources satisfying the set conditions are picosecond lasers of which the most common types are mode-locked solid-state bulk lasers and mode-locked fiber lasers [37]. A picosecond fiber laser is present at the University of Tartu Institute of Physics Laboratory of Physical Optics, where this experiment is designed.

2.1.2 Fianium WhiteLase Supercontinuum Fiber Laser

Fianium WhiteLase Blue-enhanced High Power Supercontinuum Fiber Laser model SC400-4-PP-03, is a white light laser used as the light source in the experiment. With a pulse-width of nearly 30 picoseconds and variable repetition rates of 0.1, 0.2, 0.5, 1, 2, 5, 10, 20 and 40 MHz, the laser exhibits favourable parameters for the purposes of the proposed experiment. Thus, at a repetition rate of 5 MHz and assuming a sufficient output power, the theoretical detection range limit for the supercontinuum laser is ~ 30 m with a maximum theoretical depth resolution of ~ 9 mm. Furthermore, the laser outputs a trigger pulse using nuclear instrumentation module (NIM) negative true logic standard at -0.8 volts.

2.1.3 Selection Criteria for the Spatial Light Modulator

The spatial light modulator (SLM) in the proposed experiment must have the capability to create orthogonal patterns from incident light. The maximum theoretical spatial resolution of an image acquired using computational ghost imaging is determined by the resolution of the projected patterns, thus setting the SLM’s resolution as one the key parameters for the purposes of the proposed experiment and potential future experiments. The projector’s pattern rate – frequency of changing patterns – is one of the factors potentially limiting for the image acquisition speed of a ghost imaging system. Any SLM also entailed the requirement of having ready-to-use peripheral hardware and software to facilitate its immediate use. Searching for suitable SLM’s revealed that Texas Instruments (TI) provided the most market-ready solutions, as their devices could be acquired as evaluation modules with all the suitable electrical interfaces and software. Thus, the device was selected amongst TI products which had suitable characteristics for the given experiment 2.1.

TABLE 2.1: Parameters of Texas Instrument’s DLP-series SLM evaluation modules [38]

Device	DLP4500EVM	DLP6500EVM	DLP9000EVM	DLP9500EVM
Refresh rate (Hz)	4220	9523	14989	23148
Resolution	912×1140	1920×1080	2560×1600	1920×1080
Cost (\$)	1299	1999	5749	3999

2.1.4 Digital Micromirror Device DLP Lightcrafter™ 6500

The digital micromirror device (DMD) DLP Lightcrafter™ 6500 is a spatial light modulator (SLM) developed by Texas Instruments selected for use in the proposed experiment. It can modulate the direction, amplitude and/or phase of incident light. The core of DLP Lightcrafter™ 6500 is a 1920 x 1080 micromirror (MM) array with a specified MM-array diagonal of 16.51 mm and pitch of 7.56 μm . DLP Lightcrafter™ 6500 is designed to be used with Texas Instruments designed DLP900 digital controller, which is specified to enable the DMD a pattern projection frequency of up to 9523 Hz. Both, the DLP900 and the DLP Lightcrafter™ 6500 are present on the DLP Lightcrafter™ 6500 Evaluation Module selected in this thesis [39].

The individual aluminium micromirrors (Figure 2.3) of the DLP Lightcrafter™ 6500 can be digitally controlled to assume one of two angular positions α and $-\alpha$, which are relative to the micromirror array plane. The positions of the micromirrors is altered synchronously with the micromirror's clock. The average time specified for the micromirrors to assume their ordered position is 2.5 μs [39].

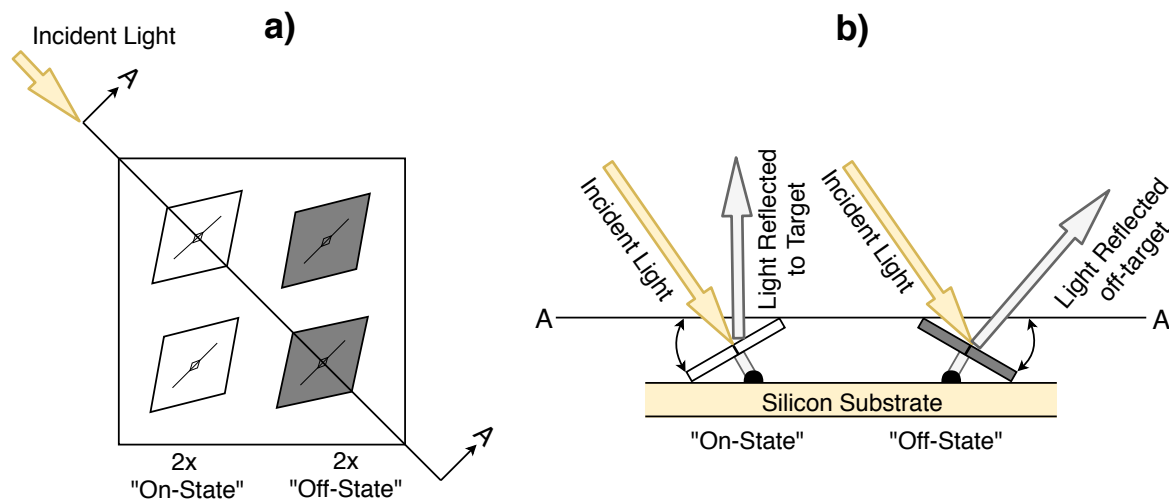


FIGURE 2.3: **a)** a 2 x 2 micromirror segment, where two of the micromirrors have been switched to α position (On-State) and the other two to $-\alpha$ position (Off-State). **b)** light incident on the On-State micromirrors is reflected towards the target to be illuminated, while the Off-State micromirrors direct the light away from the target [39].

For displaying pattern sequences, DLP Lightcrafter™ 6500 is operated in one of three modes – the Video Pattern Mode, Pattern On-The-Fly Mode and the Pre-Stored Pattern Mode. The Video Pattern Mode enables the streaming of predefined patterns from a video source, while the Pattern On-The-Fly Mode allows uploading patterns to the internal memory of DLP900 digital controller using USB or I²C. The Pre-Stored Pattern Mode pattern sequencing using images stored in the internal memory of DLP900. The DLP900's internal memory has the capacity for up to 400 1-bit patterns which can be displayed at

maximum frequency of 9523 Hz [40]. In the Pre-Stored Pattern Mode and the Pattern On-The-Fly Mode a pattern sequence's timing can be controlled externally via 3.3 V or 1.8 V logic signals (Figure 2.4). Due to interrupt processing and time used for sequence setup from the time an external trigger occurs, the maximum pattern display frequency for externally triggered patterns is 8333 Hz [41].

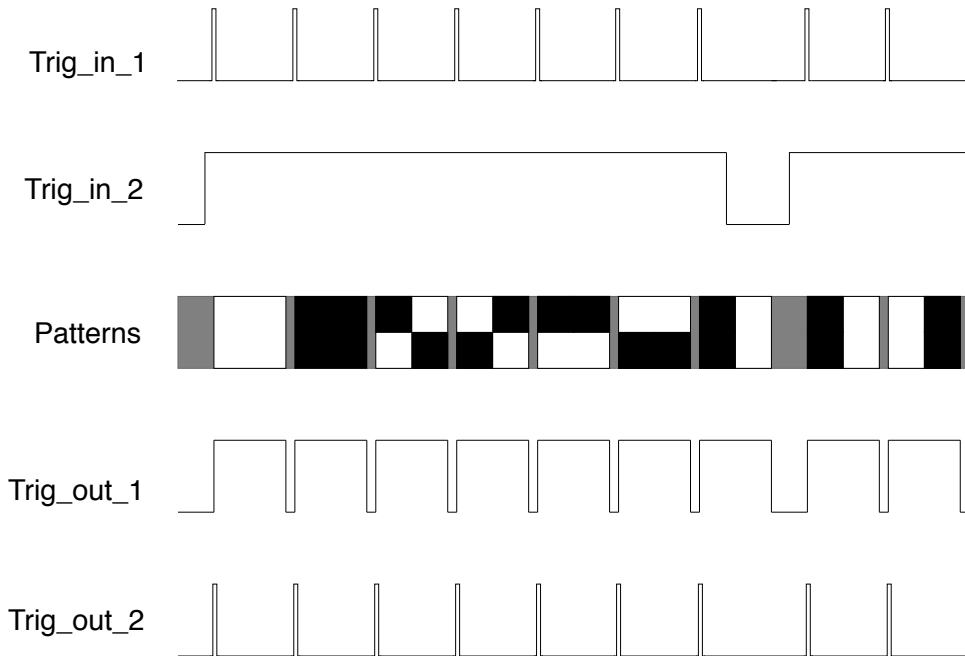


FIGURE 2.4: The DLP LightcrafterTM 6500 exhibits two trigger inputs and two trigger outputs. A pulse on the *Trig_in_1* commands the DLP900 to proceed to the next pattern. The *Trig_in_2* initiates or stops the pattern sequence. The *Trig_out_1* expresses the display duration of the pattern, while the *Trig_in_2* expresses the start of a displayed pattern. Note that if no dark time is specified between consecutive patterns, the *Trig_out_1* is high for the entire display duration of the patterns [40].

2.2 LinoSPAD

LinoSPAD is a photonic line sensor [42] designed at Delft University of Technology and at École Polytechnique Fédérale de Lausanne that is, among other applications, suitable for use in structured light experiments. The principal components of LinoSPAD are the 256 element 1-dimensional array of Geiger-mode avalanche photodiodes (GMAPDs) and the FPGA-based 64 time-to-digital converters (TDCs), which allow the detection of incident individual photons along with their relative arrival times. The photon arrival times are depicted using histograms, where detected and timestamped photons are sorted into time-bins. The sensor has an estimated dead time of approximately 100 ns, which can be coarsely tuned by changing the quenching voltage V_Q . The sensor is spectrally sensitive in the range of 400 to 850 nm, with the photon detection probability (PDP) peak of 25-35% (depending on the GMAPD bias voltage V_{OP}) at approximately 500

nm [43]. The statistical mean theoretical timing resolution of the TDCs is specified as approximately 20 ps [44]. In practice, only the delay of delay line primitives comprising of four delay chain elements can be measured and although, on average, the delay per four delay elements is $80 \text{ ps} \times \sqrt{2}$, it is not uniformly divided between the elements [45].

The electronics of LinoSPAD are implemented on two printed circuit boards. The FPGA, power regulator integrated circuits (ICs), memory ICs and the Cypress FX3 USB controller are implemented on the LinoSPAD mainboard. The GMAPDs are implemented on the LinoSPAD chip, which is installed on the LinoSPAD daughterboard [42].

2.2.1 LinoSPAD Firmware

Three versions of the LinoSPAD FPGA-based firmware have been made available [46]. These versions provide the functionality of timestamp collection from the GMAPD-events, histogram generation, pixel intensity generation using intensity counters and histogram post-processing for correcting the delay-line's fundamental non-linear properties [47]. However, due to the reasons described in Chapter 2.4.1, LinoSPAD's designer, Samuel Burri, released another version of the firmware. The new version has discarded histogram generation, pixel intensity generation and histogram post-processing primarily in order to add an additional, the 65th TDC. The following description of the LinoSPAD firmware describes the 65 TDC version of the firmware [48].

LinoSPAD firmware (Figure 2.5) is implemented on the Xilinx Spartan 6 LX FPGA. The firmware realizes the TDCs connected to the LinoSPAD chip, generation and distribution of various clock signals, synchronization circuitry and handles the commands sent to the LinoSPAD from a personal computer (PC) via the USB interface [44].

A fixed digital clock manager provides a 100 MHz frequency to the programmable clock generator, the USB transceiver and to the GMAPD event counting circuit from a 48 MHz crystal oscillator. The TDCs require a constant clock frequency of 400 MHz for sampling the delay-lines. This is generated by the phase-locked loop (PLL) from input frequency range of 20 to 100 MHz provided by a programmable clock generator [44].

The memory blocks in the FPGA cannot be clocked by the 400 MHz clock and thus a rate reduction module is implemented after timestamp collection which synchronizes the timestamp values collected at 400 MHz clock to 133 MHz clock. Furthermore, the clock architecture provides a configurable reference output frequency for use cases where the LinoSPAD is used as a master to an illumination source [49].

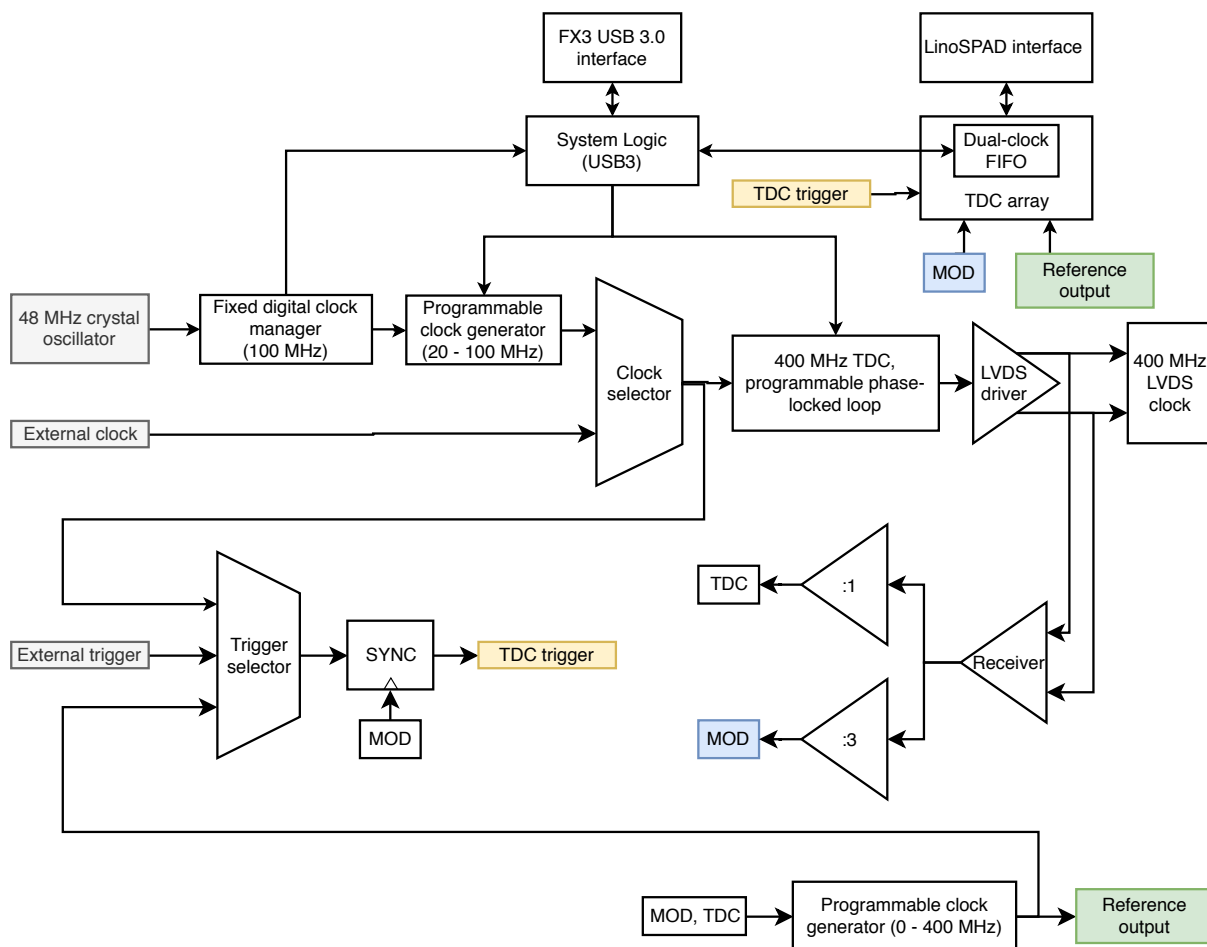


FIGURE 2.5: LinoSPAD allows for both internal and external clock sources as inputs to the PLL. Providing a suitable external clock synchronizes the LinoSPADs timestamping processes with the external clock source. The external clock source will similarly have to supply a clock at a frequency between 20 to 100 MHz [47].

A LinoSPAD TDC measures the time interval between a LinoSPAD clock event and a GMAPD event, which in an ideal case is always due to an incident photon. The primary component of the TDC is the delay line (Figure 2.6), which starts generating output code at relatively uniform time-intervals relative to an internal or external clock event and stops generating code when a GMAPD-event occurs. A single TDC is shared by four GMAPDs and a state-machine is used to connect a selected pixel to the delay line. The timestamp output from a LinoSPAD TDC has a time span of 7.5 ns, which is expanded to up to 4.8 ms using a 28-bit coarse counter clocked at 133 MHz [49]. In contrast to the first 64 TDCs, the 65th TDC is connected to non-GMAPD inputs, which, among other functions, enables acquiring timestamps from asynchronous external signals [48].

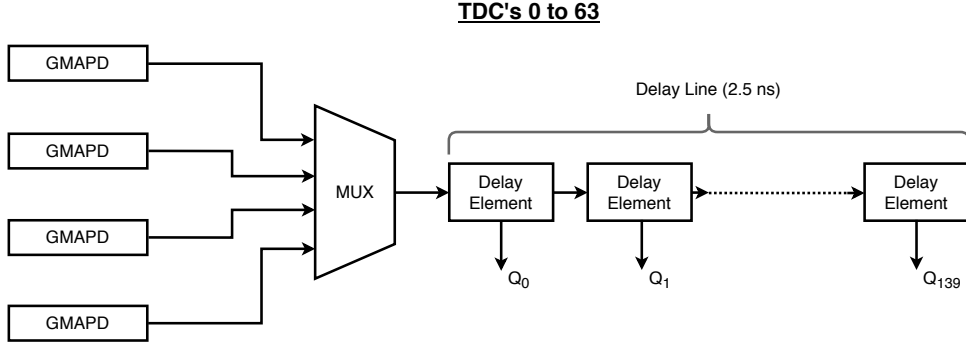


FIGURE 2.6: The 2.5 ns delay line is comprised of 140 delay elements. In order to produce binary timestamps, the outputs of the delay elements are relayed to modified thermometer-to-binary decoder, which converts the result to a binary timestamp [44].

2.2.2 Post-Processing

Due to the hardware-intrinsic uneven delay-chain durations, the raw timestamp-provided time-bins acquired by the LinoSPAD's firmware have to be normalized (Figure 2.7) by statistically dividing detected photons between time-bins. Given an input histogram H_{in} , where $k = 140$ bins covers a $\tau_{TDC} = 2.5$ ns period, we assign each raw bin a size $S_{in,i}$ and a position $P_{in,i}$, which are calculated from the histogram counts $C_{in,i}$ as

$$S_{in,i} = \tau_{TDC} \times \frac{C_{in,i}}{\sum_{j=0}^k C_{in,j}} \quad (2.3)$$

and

$$P_{in,i} = \sum_{j=0}^i S_{in,j}, \quad (2.4)$$

where i is from 0 to k [49].

For acquiring a normalized histogram with N bins sized $S_{in,i} = S_{out} = \frac{\tau_{TDC}}{N}$ and positioned at $P_{in,i} = i \times \frac{\tau_{TDC}}{N}$, an $N \times k$ correction matrix M is calculated as

$$P_{i,j} = \max\left(0, \frac{\min(P_{in,j} + S_{in,j}, P_{out,i} + S_{out,i}) - \max(P_{in,j}, P_{out,i})}{S_{in,i}}\right), \quad (2.5)$$

where the correction matrix M 's elements coincide with the overlap of the input and output histogram bins. The resulting histogram H_{out} is expressed as

$$H_{out} = M \times H_{in} [49]. \quad (2.6)$$

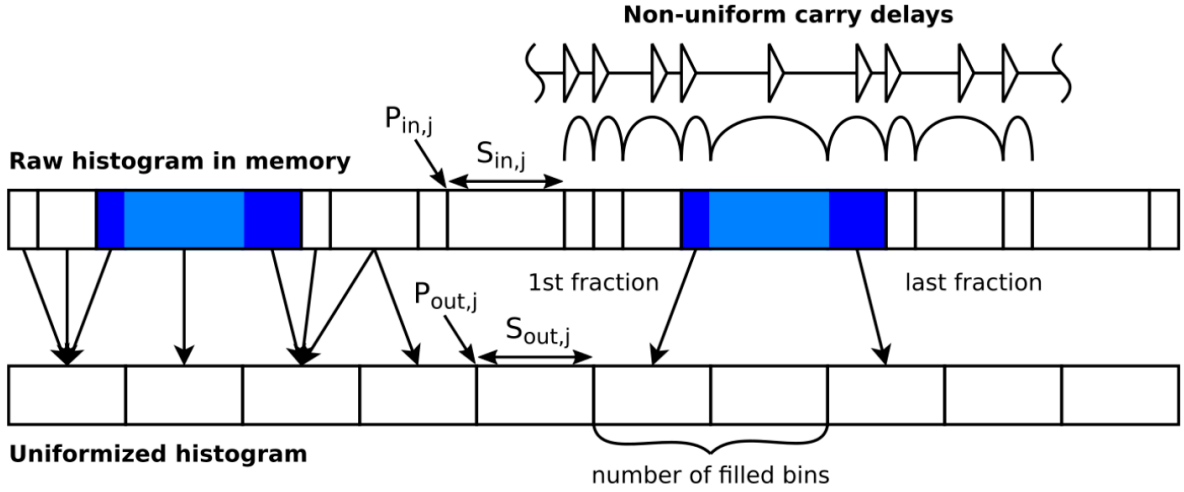


FIGURE 2.7: Multiplication of a raw histogram sized k by the correction matrix M aligns the histogram to the corrected histogram of size N by redistributing the counts (Figure by Samuel Burri [49]).

2.3 Simulations

In order to have a better understanding of the suitable lighting conditions for the experiment and to study the effects of over- and underexposing a GMAPD-detector and its respective effect to image reconstruction, photon budget calculations, shot noise simulation and GMAPD dead time simulation were conducted. In addition, where noted, measured supercontinuum laser's power fluctuations were incorporated into simulations to assess its effects on the experiment. Followingly, the details of their methods and results are discussed.

2.3.1 Photon Calculations

To calculate a preliminary estimation of the photon count conditions present at the proposed setup (Figure 2.1), light power incident at three locations was measured – light power incident on the beam expander, light power 15 centimetres from the lens at the DMD's output and. The supercontinuum laser was operated at a repetition frequency of 5 MHz and Thorlabs PM100D optical power meter with Thorlabs S401C and S120C detectors were used. This data enabled the approximation of visible (400-850 nm) light power incident on a single pixel. This result combined with the supercontinuum laser's spectrum

data and LinoSPAD's photon detection probability (PDP) yielded the end result of one LinoSPAD's pixel receiving approximately 23360 photons per 100 nanoseconds. This result allows the conclusion that the proposed setup provides sufficient illumination for the experiment and exhibits light intensity reserves for either reducing the supercontinuum laser's repetition rate or for placing the object to be imaged farther from the DMD and the LinoSPAD.

2.3.2 Shot Noise Simulation

Photon shot noise is a phenomenon that manifests due to discrete photon emissions from a light source occurring at random times. As the intensity of light incident on an object decreases, the difference in the individual photon's arrival times becomes more significant [32]. Photon counting devices are almost shot-noise limited [50] and as shot noise induced light intensity fluctuations may have a significant effect on the quality of the reconstructed image in the proposed experiment, its effects are assessed in a simulation. To simulate the effect of shot noise on image reconstruction quality in the proposed experiment, computational ghost imaging algorithm was simulated. This required implementing Hadamard matrices generation and generating the signals which would be later used for reconstructing the image. The simulated target object was chosen as a 256×256 image for simplicity – as the LinoSPAD itself is a 256×1 GMAPD-array, due to which a total of 512 patterns (256 patterns with their respective inverse patterns) need to be generated. Signals are generated using the original target object (with its pixel values normalized to between 0 and 1 as the reflectivity value of the object), the Hadamard-based patterns generated earlier, measured and normalized laser power fluctuations and the tuning parameter. The tuning parameter is specified as the main variable of the modelling and it represents the average number of photons detected by the detector per pattern per pixel ($\frac{\text{photons}}{\text{pattern} \times \text{pixel}}$). Shot noise itself can be modelled as a Poisson process [51]. Poisson distributed random samples are created with the Poisson expectation of interval, which is the tuning parameter. The resulting numbers are the simulated signal values and can be used for reconstructing the signal. The simulation results (Appendix A) indicate that shot noise has a significant effect on image reconstruction in cases where photon rate is below $5000 \frac{\text{photons}}{\text{pattern} \times \text{pixel}}$.

2.3.3 Detector Dead Time Simulation

The dead time of a GMAPD-detector was simulated by generating each photon detected by each pixel of the detector for each pattern independently and subsequently comparing the detection times of each photon to determine if the photon arrived during a specified detector dead time. A photon arriving within the dead time of a previous detection would not be counted. The arrival times for events in a Poisson process are governed by exponential distribution. The number of generated photons was specified by the tuning parameter $\frac{\text{photons}}{\text{pattern} \times \text{pixel}}$, which can be related to the object's distance, and set pattern duration, which controls the total amount of photons that can be counted. The dead time length used in the simulation was 100 ns. The resulting image was reconstructed using

signal values acquired by counting each individual photon per pixel per pattern. Multiple simulation runs with different tuning parameter values were conducted and mean-square error (MSE) and structural similarity index (SSI) algorithms were used to assess the difference between the original image and the reconstructed image (Figure 2.8). The simulated reconstructed images are shown in appendix B. It can be clearly seen, that overexposing the object results in deteriorated image quality as majority of the photons remain undetected and information is lost. An additional interesting phenomenon can be observed from the detector dead time simulations. Beyond the point of severe deterioration of the reconstructed image from increasing number of undetected photons, the reconstructed image seems as if it is inverted (Appendix C).

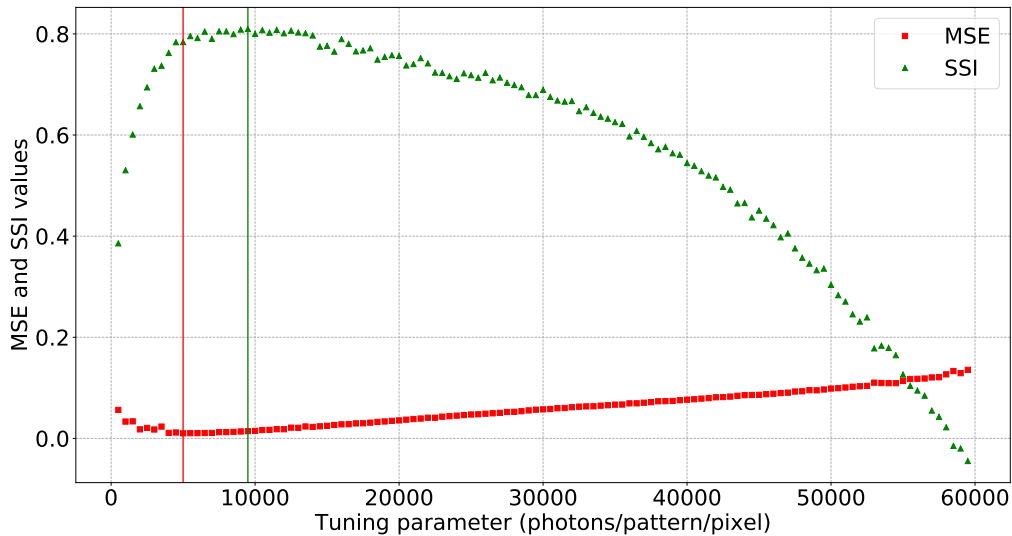


FIGURE 2.8: The tuning parameter optimum was found by running the dead time simulation algorithm using tuning parameter values between 0 to 60000 with a step of 500. Comparison using the MSE algorithm detected highest similarity between the reconstructed image and the original image with a tuning parameter value of 5000 $\frac{\text{photons}}{\text{pattern} \times \text{pixel}}$. The SSI algorithm recognized highest similarity between the images at the tuning parameter value of 9500. Note that due to heavy computational load, this simulation was run using 64×64 target objects.

2.4 System Setup

The experiment setup (Figure 2.9) for implementing ghost imaging algorithms using LinoSPAD as the detector consists of five principal components. A Fianium WhiteLase High Power Supercontinuum Fiber Laser and a DLP Lightcrafter™ 6500 digital micromirror device (DMD) with conditioning optics are used for projecting the Hadamard matrix-based patterns on to an object. The light diffusely reflected from the object is incident on the LinoSPAD and in addition, a trigger signal correlated to the light pulses

from the laser is connected to the LinoSPAD. A microcontroller is used to trigger the pattern progression on the DMD using 3.3 V logic and the DMD-provided output trigger signals (Figure 2.4) can be used in the control process of the experiment. Both the LinoSPAD and the microcontroller are interfaced to a personal computer, which handles the control and data acquisition of the setup.

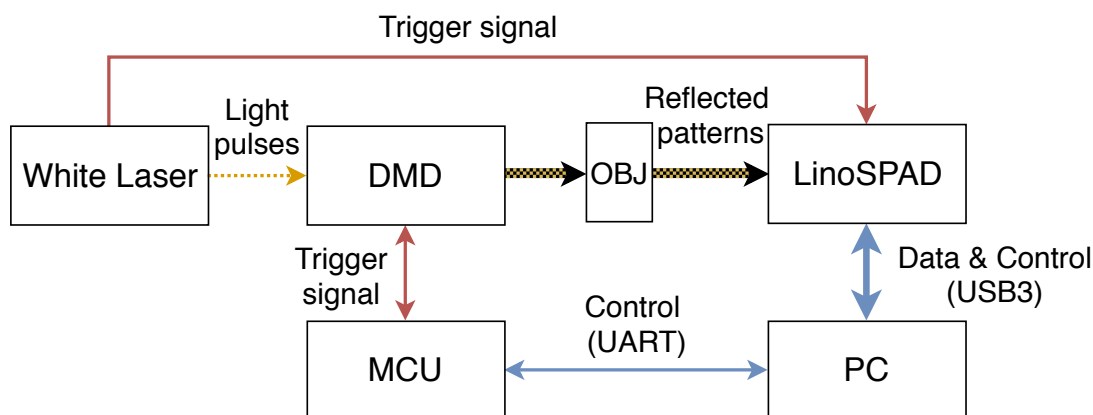


FIGURE 2.9: The trigger signal from the supercontinuum laser is fed to the 65th TDC of the LinoSPAD instead of its external clock input. This is due to the supercontinuum laser’s unsuitable fundamental trigger frequency of 38.1 MHz , which does not allow the LinoSPAD’s PLL to lock on to the signal (Chapter 2.4.1).

Timestamps acquired from the 65 TDC’s are relative to the internal clock of the LinoSPAD. To acquire any meaningful data, the timestamps from the GMAPDs that are acquired from a laser’s single pulse will have to be correlated to the timestamp of the pulse (Figure 2.10).



FIGURE 2.10: The phase shift between the laser’s pulse and a detected photon can be obtained by subtracting the laser pulse’s timestamp from the timestamp of the detected photon. This subtraction has to occur between timestamps acquired within a period of f^{-1} , where f is the laser’s pulse repetition frequency.

Control Software

The software for controlling the experiment consists of three parts – LinoSPAD firmware which fills the role of acquiring timestamps from the LinoSPAD chip, microcontroller (MCU) firmware which provides an interface for accessing the triggering logic on the micromirror device and lastly software on the PC which governs over the other two firmware, provides the endpoint to the experiment results and offers a user interface for controlling the experiment parameters and its initiation (Figure 2.11).

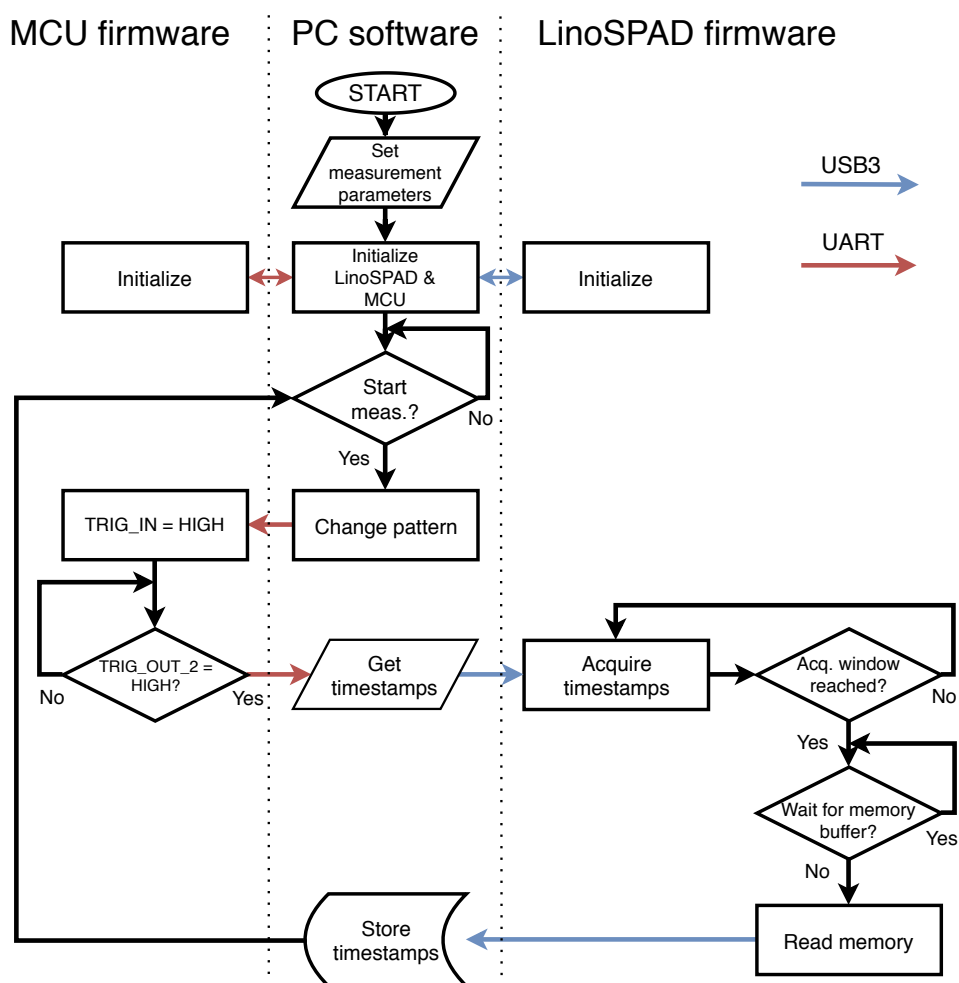


FIGURE 2.11: The depicted process is maintained until a desired amount of timestamps have been recorded. Subsequently, the timestamps are used in post-processing, where the inherent time-bins are equalized. Resulting data can then be used in a computational ghost imaging algorithm for reconstructing the image.

2.4.1 Setup Tests

Preliminary tests with the selected devices to confirm the technical feasibility of the proposed design were conducted. Specifically, the interoperability of LinoSPAD and the

supercontinuum laser needed to be ascertained. In addition, the triggering of the proposed DMD was tested.

In order to be able to use the supercontinuum laser's trigger signal as an input to the LinoSPAD, the laser trigger's NIM logic level has to be converted to match the LinoSPAD's required 5 V TTL logic. A G5-48 pulse generator [52] was used to resolve this, as it was capable of creating TTL-logic compatible pulses and accepted negative voltage as input. The supercontinuum laser's trigger was fed to the pulse generator's trigger input and G5-48's output supplied the converted trigger signal to the LinoSPAD. Initially, this solution was sufficient as it enabled the testing of LinoSPAD's triggering mechanisms.

At first, comparing the parameters of the LinoSPAD and the supercontinuum laser showed that it was possible to provide the laser's output trigger as an external clock input to the LinoSPAD (Figure 2.5). This would mean that the laser's trigger would represent the reference time against which detected photons would be timestamped. Regrettably, the attempt to employ laser's trigger as the external clock signal for the LinoSPAD was unsuccessful. This was due to the supercontinuum laser's actual fundamental repetition frequency being 38.1 MHz and thus the desired 20 MHz frequency was, in reality, approximately 19.08 MHz. This resulted in LinoSPAD's phase-locked loop being unable to lock onto the signal using it as an external clock. As a possible solution an option, where the supercontinuum laser's repetition rate would be altered by its manufacturer, was considered. However, this was discarded due to the procedure's price. Although LinoSPAD is capable of providing an output trigger for externally triggering a light source, the supercontinuum laser does not facilitate this function and thus this solution could also not be used.

By contacting one of the LinoSPAD's designers, Samuel Burri, a potential solution was found by altering the LinoSPAD's firmware by adding another time-to-digital converter and discarding a significant portion of its other features (described in chapter 2.2). With this approach (described in chapter 2.4), it was possible to acquire meaningful data from the LinoSPAD. This required implementing the post-processing of raw histograms from the acquired timestamps and the calculations of final timestamps correlated to the laser's trigger. The acquired results allowed a preliminary assessment of the triggering quality of the system setup. The initial results showed that although correlated to the laser's trigger, the measured photons would seemingly arrive over a period of nanoseconds. This was likely to be due to timing jitter (Figure 2.12) – timing delay deviation, from the trigger signal chain, due to the reason, that the light beam was not conditioned in any way after emission from the laser and the target object was positioned approximately 0.5 m from the LinoSPAD and had no depth.

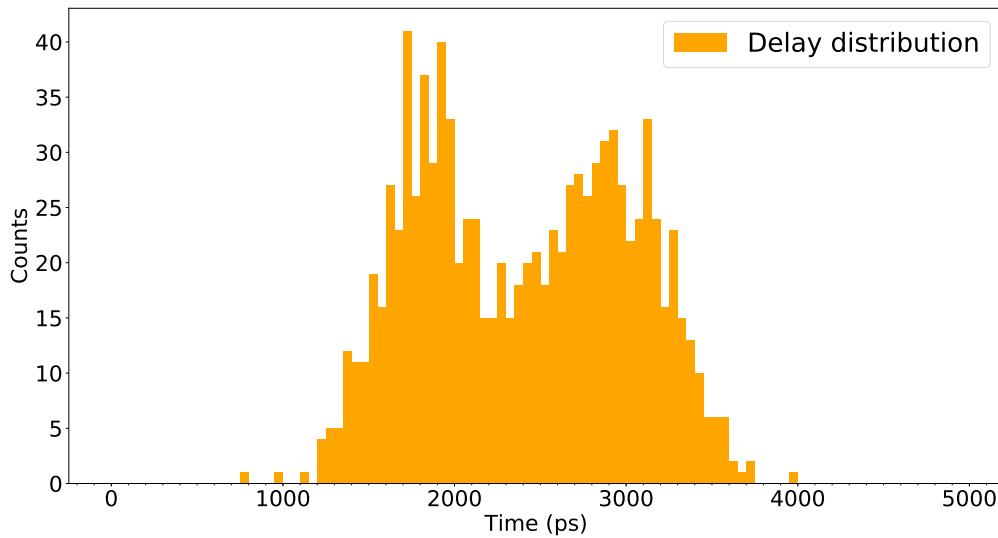


FIGURE 2.12: Delay distribution between laser's output and G5-48 pulse generator output shows two distinctive peaks with an approximate distance of 1250 ps. The data used in the figure was obtained with a Lecroy WaveRunner 6000A Series oscilloscope.

Preliminary analysis suggested that the G5-48 was introducing the observed jitter into the trigger signal chain. Instead of the G5-48, Ortec Model 9327 amplifier and timing discriminator was used as a device facilitating NIM to TTL conversion. The device is designed to be used in low-jitter picosecond applications, as it uses methods for reducing the effects of noise and signal rise time to timing jitter [53]. While replacing the G5-48 enhanced the timing conditions (Figure 2.13), for the given experiment this was insufficient.

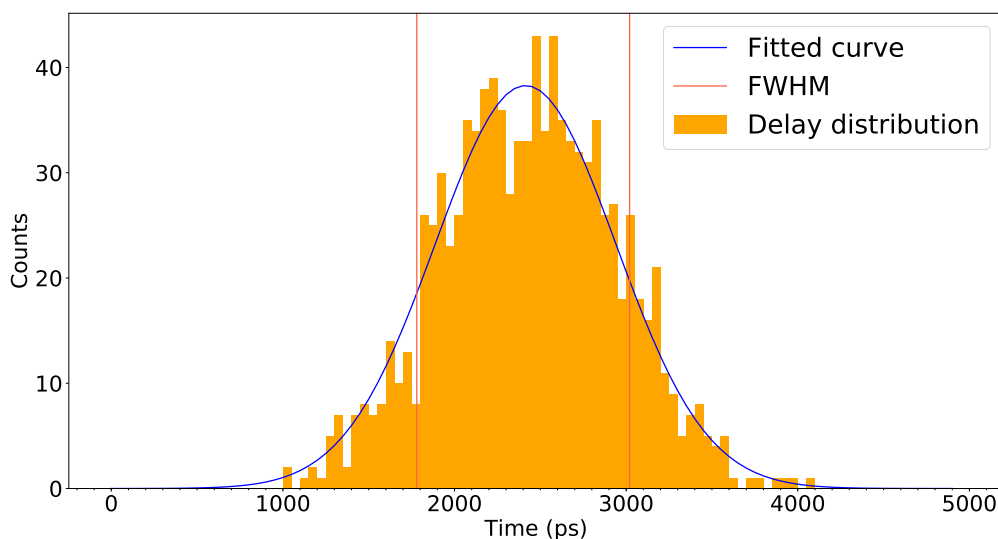


FIGURE 2.13: Delay distribution between laser’s output and Model 9327 shows slightly improved timing conditions, as a Gaussian function can be differentiated. Regardless, the full width at half maximum (FWHM) of the distribution is nearly 1.25 ns. The data used in the figure was obtained with a Lecroy WaveRunner 6000A Series oscilloscope.

As the timing jitter between the supercontinuum laser’s light output and its electrical trigger output was unknown, an alternative triggering scheme (Figure 2.14) was used. Supercontinuum laser’s electrical trigger was not used and instead the trigger signal was created by using a photodiode to produce a pulse from the laser’s light.

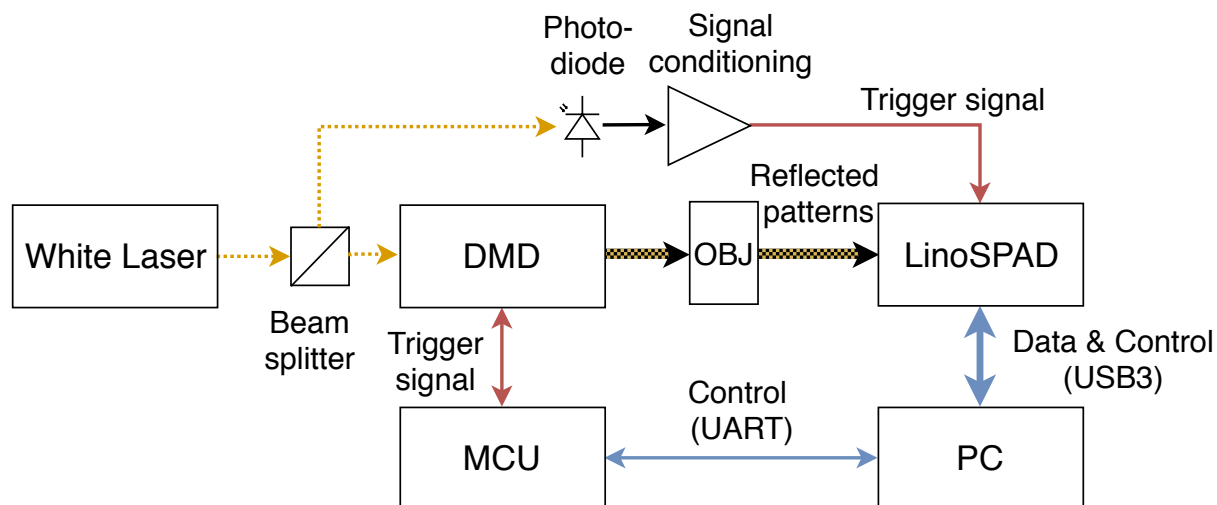


FIGURE 2.14: A beam splitter was used to guide the light from the laser to a photodiode. The resulting photocurrent was conditioned to TTL-logic levels and supplied to the LinoSPAD.

Opting to use the photodiode-generated trigger resulted in significantly improved timing conditions (Figure 2.15). Still, the expected limit of LinoSPAD's time resolution of ~ 100 ps was not reached, implying that triggering circuitry can be further optimized.

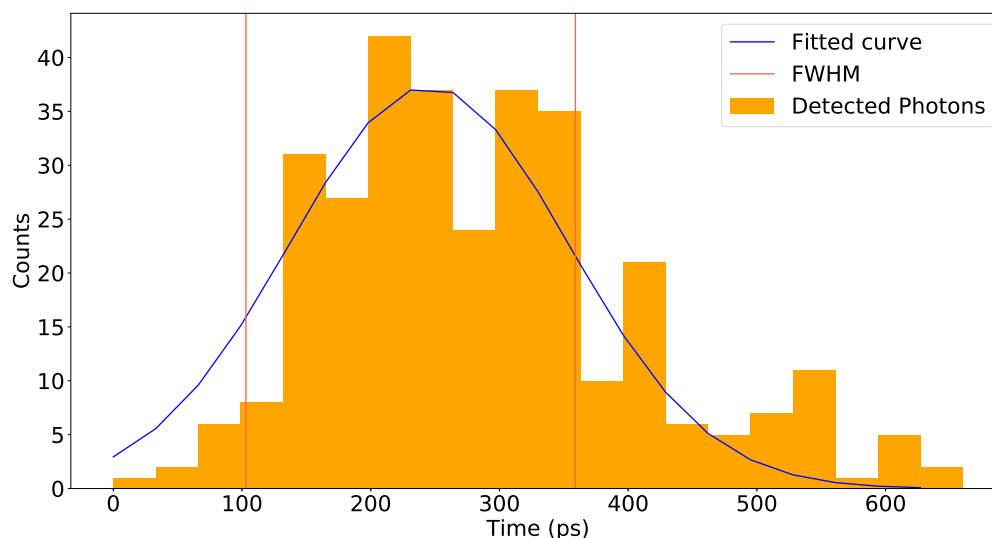


FIGURE 2.15: LinoSPAD detected photons form a laser pulse with a full width at half maximum (FWHM) value of 256 ps. Figure is ranged to show only the detected pulse.

Additionally, controlling the DMD's pattern sequencing via its trigger interface was tested. An STM32F103C8 microcontroller based development board "Blue Pill" was interfaced via its GPIO's to the DMD's input and output trigger pins. The development board was connected to a personal computer via UART and controlled via custom-written C++ software. Using this setup it was possible to successfully manage DMD's pattern sequencing.

Conclusion

Computational ghost imaging is a promising method for future imaging technologies. One of the complications hindering the feasibility of single-pixel computational ghost imaging in many practical applications is its time requirement for obtaining an image with sufficient quality. As the desired spatial resolution of the object to be imaged increases, the amount of patterns projected onto the object increases significantly. This fundamental trade-off of a single-pixel computational ghost imaging device forces the system to either longer image acquisition durations or a low spatial resolution reconstruction of the image.

The aim of this thesis was to develop a proof-of-principle novel experiment design for implementing a Geiger-mode avalanche photodiode array in a direct time of flight 3D computational ghost imaging setup in order to achieve notably shorter image acquisition times without making a compromise in the quality of the reconstructed image. The LinoSPAD line sensor is the core element used in the proposed experiment setup and it incorporates a 256×1 array of Geiger-mode avalanche photodiodes, each of which is interfaced to a time-to-digital converter and thus allowing the simultaneous capture of depth data in addition to image data. By dividing the computational ghost imaging system's field of view between LinoSPAD's individual pixels, it is possible to dramatically reduce the acquisition time of the 3D-image.

The thesis covered the theoretical background of ghost imaging and its aspects, the suitability of various photodiodes in computational ghost imaging applications and gave an overview of primary 3D-imaging technologies. The proposed design of the experiment focused on its optical setup and its critical sub-components – the light source, light projector and the LinoSPAD sensor. The primary selection criteria for the light source and the light projector were defined. The LinoSPAD's operational aspects were thoroughly studied and the resulting requirements for the design were considered. In addition, supplementary simulations relevant for a more profound comprehension of the experiment's conditions were performed. Lastly, a system setup incorporating the triggering scheme and experiment control software architecture was devised and preliminary setup tests were conducted.

Conformingly to the selection criteria, a suitable light source – the Fianium WhiteLase Supercontinuum Fiber Laser – and a suitable light projector – the Digital Micromirror Device DLP LightcrafterTM 6500 – were selected as the pattern projection components of the experiment. Although preliminary attempts to use the white laser's output trigger as an external clock for triggering the LinoSPAD's timing circuitry were unsuccessful, altered firmware for the LinoSPAD provided by its designer allowed the acquiring of photon timestamps correlated to the white laser. The timing jitter initially introduced into the

system by a pulse generator converting logic level voltages between the laser's output trigger and the LinoSPAD, was significantly improved by discarding the supercontinuum laser's electrical trigger signal and acquiring the laser's trigger via photodiode-generated pulse from the laser's light output. Regardless, the full time resolution of LinoSPAD was not achieved. The simulation results showed that a photon counting ghost imaging setup is vulnerable to shot noise in low detected photon rates. However, detector dead time simulations indicated that a reconstructed image suffers from severe drop in quality in the presence of too high rate of photons incident on a detector.

LinoSPAD is a promising new type of sensor, which could significantly accelerate the progress of computational ghost imaging based 3D-imaging systems. However, due to extremely strict timing requirements, sufficient attention must be given to triggering circuitry. Furthermore, relatively meticulous demands for the light source's pulse width may complicate the development of direct time of flight based 3D ghost imaging systems. Nevertheless, the potential of single-photon sensitivity detectors and computational ghost imaging methods is apparent and both fields are likely candidates for accelerated development in the future.

Outlook

The results of this thesis will be used to conduct the experiment, where a 3D image is reconstructed using the proposed method. Control software described in chapter 2.4 will be created for this purpose. Furthermore, optimizations to the timing circuitry will be conducted.

Speculatively, 3D ghost imagers in general could benefit from progress made in laser technologies. Individually addressable vertical-cavity surface-emitting laser (VCSEL) arrays with suitable pulse characteristics and output power, could substitute currently used micromirror-based projectors. In addition, pattern design tailored for a specific scene from data obtained by previous measurements or even from camera data could, possibly, further lower the amount of projected patterns required for satisfactory image reconstruction.

Bibliography

- [1] The automotive lidar market. http://www.woodsidecap.com/wp-content/uploads/2018/04/Yole_WCP-LiDAR-Report_April-2018-FINAL.pdf. Accessed: 2019-05-04.
- [2] Vasyl Molebny, Paul F. McManamon, Ove Steinvall, Takao Kobayashi, and Weibiao Chen. Laser radar: historical prospective from the East to the West. *Optical Engineering*, 56(3):1 – 24 – 24, 2016. doi: 10.1117/1.OE.56.3.031220.
- [3] *Velodyne LiDAR Puck LITE Brochure*. URL <https://velodynelidar.com/vlp-16-lite.html>. Accessed: 2019-05-16.
- [4] *S3 Solid State LiDAR Sensor Brochure*. URL <https://quanergy.com/s3/>. Accessed: 2019-05-16.
- [5] *InnovizPro Brochure*. URL <https://innoviz.tech/innovizpro/>. Accessed: 2019-05-16.
- [6] Baraja Pty Ltd. personal communication, 2018.
- [7] Luminar Technologies, Inc. personal communication, 2018.
- [8] P. Kaldén and E. Sternå. Development of a low-cost laser range-finder (LIDAR). MSc thesis, Chalmers University of Technology, 2015.
- [9] Christian Wolff. Continuous wave radar. <http://www.radartutorial.eu/02.basics/Continuous%20Wave%20Radar.en.html>. Accessed: 2019-04-09.
- [10] Christopher V. Poulton, Ami Yaacobi, David B. Cole, Matthew J. Byrd, Manan Raval, Diedrik Vermeulen, and Michael R. Watts. Coherent solid-state LIDAR with silicon photonic optical phased arrays. *Optics Letters*, 42(20):4091–4094, Oct 2017. doi: 10.1364/OL.42.004091.
- [11] Paul F. McManamon, editor. *Field Guide to Lidar*. SPIE Press, 2015.
- [12] Keita Yasutomi, Takahiro Usui, Sang-Man Han, Taishi Takasawa, Keiichiro Kagawa, and Shoji Kawahito. An indirect time-of-flight measurement technique with impulse photocurrent response for sub-millimeter range resolved imaging. *Optics Express*, 22(16):18904–18913, Aug 2014. doi: 10.1364/OE.22.018904.
- [13] John C. Howell Daniel J. Lum, Samuel H. Knarr. Frequency-modulated continuous-wave LiDAR compressive depth-mapping. *Optics Express*, 26(12), 2018.

- [14] David S. Hall. High definition lidar system. US Patent US7969558B2, Jun 2008.
- [15] David S. Hall, Pieter J. Kerstens, and Mathew Noel Rekow. Integrated illumination and detection for LIDAR based 3-D imaging. US Patent US20190011563A1, Apr 2018.
- [16] K. H. Koh and C. Lee. A Two-Dimensional MEMS Scanning Mirror Using Hybrid Actuation Mechanisms With Low Operation Voltage. *Journal of Microelectromechanical Systems*, 21(5):1124–1135, Oct 2012. ISSN 1057-7157. doi: 10.1109/JMEMS.2012.2196497.
- [17] Y. Wang and M. C. Wu. Micromirror based optical phased array for wide-angle beam-steering. In *2017 IEEE 30th International Conference on Micro Electro Mechanical Systems (MEMS)*, pages 897–900, Jan 2017. doi: 10.1109/MEMSYS.2017.7863553.
- [18] Braden Smith, Brandon Hellman, Adley Gin, Alonzo Espinoza, and Yuzuru Takashima. Single chip lidar with discrete beam steering by digital micromirror device. *Opt. Express*, 25(13):14732–14745, Jun 2017. doi: 10.1364/OE.25.014732.
- [19] Chantelle Dubois. What is solid state lidar and is it faster, cheaper, better? <https://www.allaboutcircuits.com/news/solid-state-lidar-faster-cheaper-better/>. Accessed: 2019-04-09.
- [20] Baraja spectrum-scan lidar technology. <https://www.baraja.com/technology/>. Accessed: 2019-04-09.
- [21] P. F. McManamon, P. J. Bos, M. J. Escuti, J. Heikenfeld, S. Serati, H. Xie, and E. A. Watson. A Review of Phased Array Steering for Narrow-Band Electrooptical Systems. *Proceedings of the IEEE*, 97(6):1078–1096, June 2009. ISSN 0018-9219. doi: 10.1109/JPROC.2009.2017218.
- [22] Changsoo Je, Sang Wook Lee, and Rae-Hong Park. Colour-stripe permutation pattern for rapid structured-light range imaging. *Optics Communications*, 285(9):2320 – 2331, 2012. ISSN 0030-4018. doi: <https://doi.org/10.1016/j.optcom.2012.0.1025>.
- [23] F. Remondino and D. Stoppa. *TOF Range-Imaging Cameras*. Springer, 2013.
- [24] Miles Padgett and Robert Boyd. An introduction to ghost imaging: Quantum and classical. *Philosophical Transactions of The Royal Society A Mathematical Physical and Engineering Sciences*, 375:20160233, 08 2017. doi: 10.1098/rsta.2016.0233.
- [25] Tatum Pittman, Yanhua Shih, D V. Strelakov, and Alexander Sergienko. Optical imaging by means of two-photon quantum entanglement. *Physical review. A*, 52: R3429–R3432, 12 1995. doi: 10.1103/PhysRevA.52.R3429.
- [26] F. Ferri, D. Magatti, A. Gatti, M. Bache, E. Brambilla, and L. A. Lugiato. High-Resolution Ghost Image and Ghost Diffraction Experiments with Thermal Light. *Physical Review Letters*, 94:183602, May 2005. doi: 10.1103/PhysRevLett.94.183602.

- [27] Jeffrey H. Shapiro. Computational ghost imaging. *Physical Review A*, 78:061802, Dec 2008. doi: 10.1103/PhysRevA.78.061802.
- [28] Stephen Stewart Welsh. *Applications of single-pixel imaging*. PhD thesis, University of Glasgow, 2017.
- [29] Stephen S. Welsh, Matthew P. Edgar, Richard Bowman, Phillip Jonathan, Baoqing Sun, and Miles J. Padgett. Fast full-color computational imaging with single-pixel detectors. *Opt. Express*, 21(20):23068–23074, Oct 2013. doi: 10.1364/OE.21.023068. URL <http://www.opticsexpress.org/abstract.cfm?URI=oe-21-20-23068>.
- [30] Ming-Jie Sun, Ling-Tong Meng, Matthew P. Edgar, Miles J. Padgett, and Neal Radwell. A Russian Dolls ordering of the Hadamard basis for compressive single-pixel imaging. *Scientific Reports*, 7(10), 2017.
- [31] Ming-Jie Sun, Matthew Edgar, Graham M. Gibson, Baoqing Sun, Neal Radwell, Robert Lamb, and Miles Padgett. Single-pixel three-dimensional imaging with time-based depth resolution. *Nature Communications*, 7, 07 2016. doi: 10.1038/ncomms12010.
- [32] A. Eisele. *Millimeter-Precision Laser Rangefinder Using a Low-Cost Photon Counters*. Scientific Publishing, 2013.
- [33] Paul F. McManamon, Paul Stuart Banks, Jeffrey D. Beck, Dale G. Fried, Andrew S. Huntington, and Edward A. Watson. Comparison of flash lidar detector options. *Optical Engineering*, 56(3):1 – 23 – 23, 2017. doi: 10.1117/1.OE.56.3.031223.
- [34] Z. Ghassemlooy, W. Popoola, and S. Rajbhandari. *Optical Wireless Communications – System and Channel Modelling with MATLAB*. CRC Press, 2013.
- [35] L. Zhang, D. Chitnis, H. Chun, S. Rajbhandari, G. Faulkner, D. O’Brien, and S. Collins. A Comparison of APD- and SPAD-Based Receivers for Visible Light Communications. *Journal of Lightwave Technology*, 36(12):2435–2442, June 2018. ISSN 0733-8724. doi: 10.1109/JLT.2018.2811180.
- [36] Edward M.D. Fisher. *Principles and Early Historical Development of Silicon Avalanche and Geiger-Mode Photodiodes*. IntechOpen, 2017.
- [37] R. Paschotta. Article on picosecond lasers in the RP Photonics Encyclopedia. https://www.rp-photonics.com/picosecond_lasers.html. Accessed: 2019-05-17.
- [38] Texas Instruments. Advanced light control products. <http://www.ti.com/dlp-chip/advanced-light-control/products.html?pqs=pags&familyid=1743#p1907=DMD&sort=p1913;desc>. Accessed: 2019-05-16.
- [39] *DLP6500 0.65 1080p MVSP S600 DMD Datasheet*. Texas Instruments, 2016.
- [40] *DLPC900 Digital Controller for Advanced Light Control*. Texas Instruments, 2016.

-
- [41] *DLPC900 Programmer's Guide*. Texas Instruments, 2017.
- [42] Harald Homulle Samuel Burri. *LinoSPAD Mainboard Manual*. École Polytechnique Fédérale de Lausanne, 2016.
- [43] Samuel Burri. *LinoSPAD Camera Factsheet*. École Polytechnique Fédérale de Lausanne, 2016.
- [44] Samuel Burri, Claudio Bruschini, and Edoardo Charbon. LinoSPAD: A Compact Linear SPAD Camera System with 64 FPGA-Based TDC Modules for Versatile 50 ps Resolution Time-Resolved Imaging. *Instruments*, 1:6, 12 2017. doi: 10.3390/instruments1010006.
- [45] Sergey Omelkov. personal communication, 2019.
- [46] LinoSPAD support. <https://linospad.ch/>. Accessed: 2019-05-20.
- [47] Samuel Burri and Harald Homulle. *LinoSPAD Software Manual*. École Polytechnique Fédérale de Lausanne, 2016.
- [48] Samuel Burri. personal communication, 2019.
- [49] Samuel Burri. *Challenges and Solutions to Next-Generation Single-Photon Imagers*. Phd thesis, École Polytechnique Fédérale de Lausanne, 2016.
- [50] R.K. Henderson, B.R. Rae, and D.-U. Li. 11 - Complementary metal-oxide-semiconductor (CMOS) sensors for fluorescence lifetime imaging (FLIM). In *High Performance Silicon Imaging*, pages 312 – 347. Woodhead Publishing, 2014. ISBN 978-0-85709-598-5. doi: <https://doi.org/10.1533/9780857097521.2.312>.
- [51] Robert P. Dobrow. *Introduction to Stochastic Processes with R*. John Wiley & Sons, Inc., 2016.
- [52] *G5-48 Pulse Generator Technical Parameters*. URL <https://zapadpribor.com/en/g5-48/>. Accessed: 2019-05-09.
- [53] *ORTEC Model 9327 1-GHz Amplifier and Timing Discriminator Manual*. URL <https://www.ortec-online.com/-/media/ametektortec/manuals/9327-mnl.pdf>. Accessed: 2019-05-15.

Appendix A – Shot Noise Simulation Results

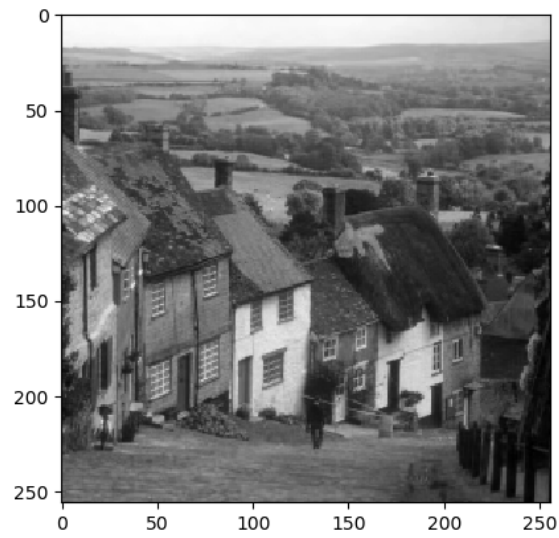


FIGURE 16: Original target object.

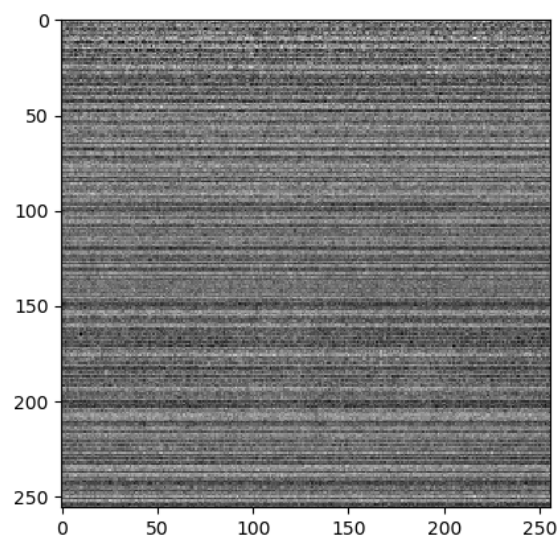


FIGURE 17: Photon rate = 100 (photons/pattern/pixel).

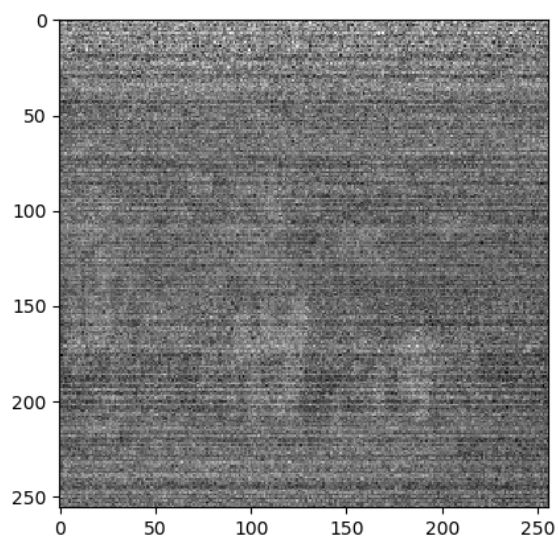


FIGURE 18: Photon rate = 500 (photons/pattern/pixel).

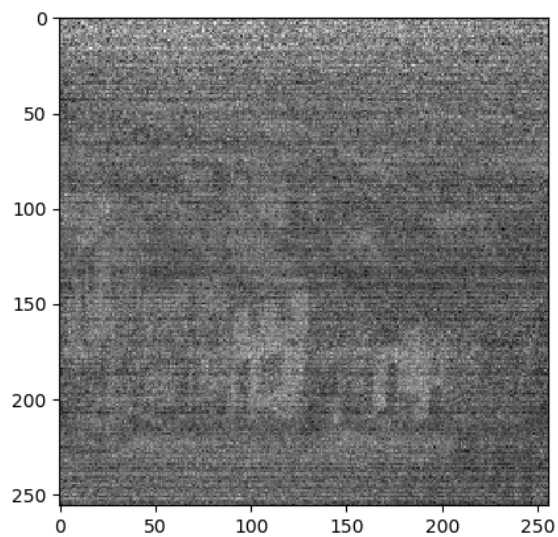


FIGURE 19: Photon rate = 1000 (photons/pattern/pixel).

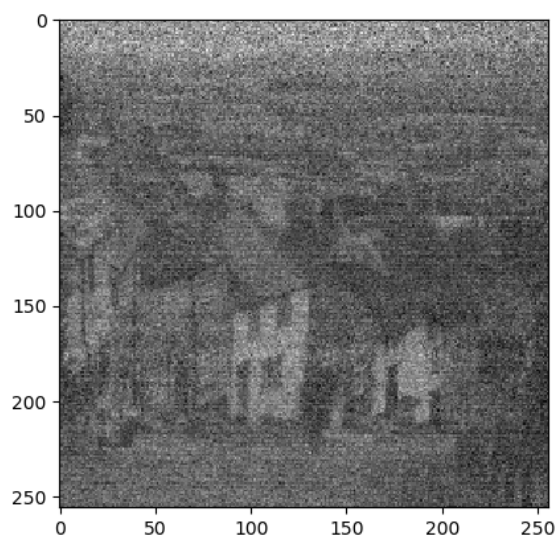


FIGURE 20: Photon rate = 2500 (photons/pattern/pixel).

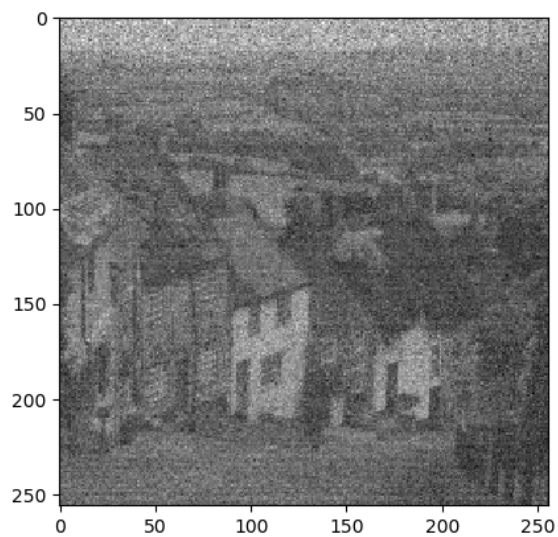


FIGURE 21: Photon rate = 5000 (photons/pattern/pixel).

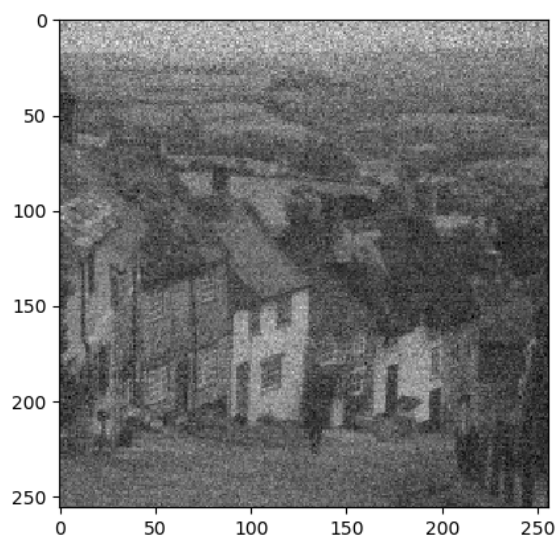


FIGURE 22: Photon rate = 7500 (photons/pattern/pixel).

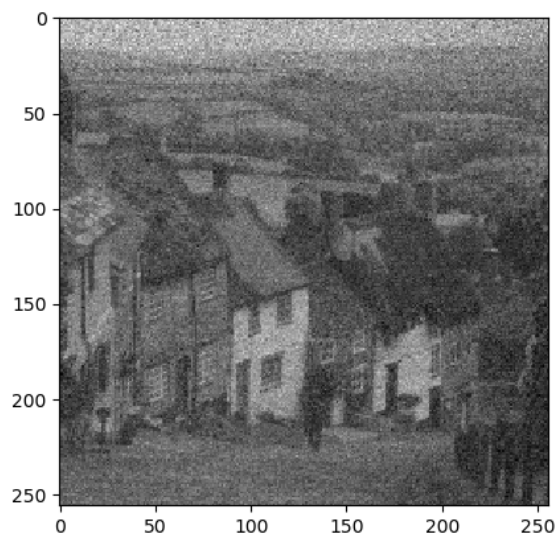


FIGURE 23: Photon rate = 10000 (photons/pattern/pixel).

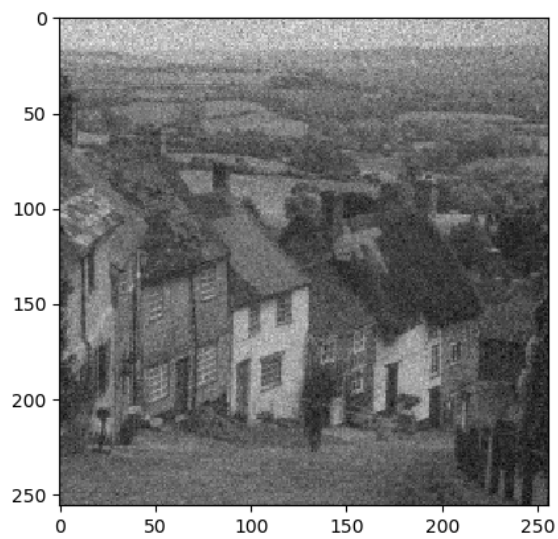


FIGURE 24: Photon rate = 20000 (photons/pattern/pixel).

Appendix B – Dead Time Simulation Results

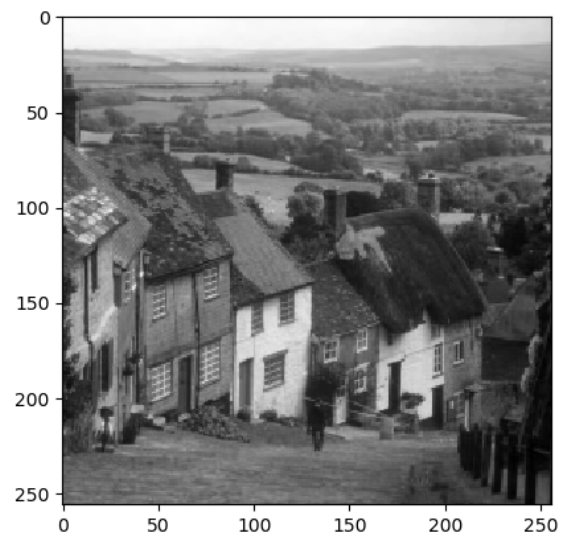


FIGURE 25: The original target image with the resolution of 256x256.

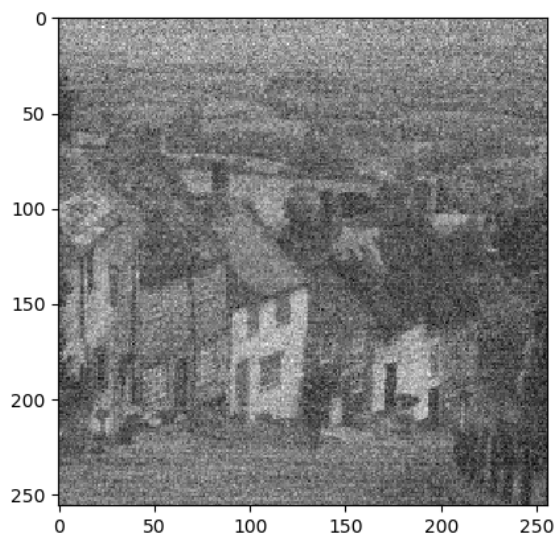


FIGURE 26: Reconstructed image with a photon rate of 6250 photons per pattern. Pattern duration is 1 ms. The amount of detected photons is 1147 and the amount of undetected photons due to dead time is 188.

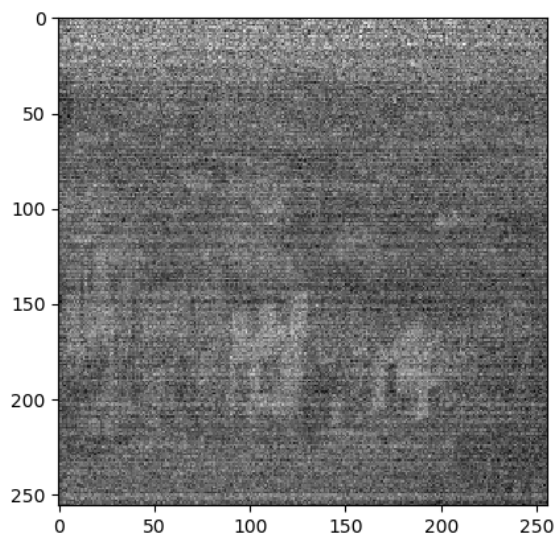


FIGURE 27: Reconstructed image with an underexposing photon rate of 1000 photons per pattern. Pattern duration is 1 ms. The amount of detected photons is 208 and the amount of undetected photons due to dead time is 5. It can be seen that the signal is too weak for image reconstruction.

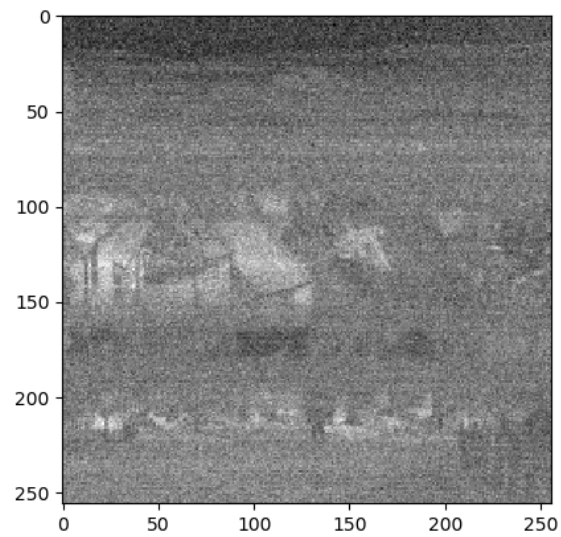


FIGURE 28: Reconstructed image with an overexposing photon rate of 50000 photons per pattern. Pattern duration is 1 ms. The amount of detected photons is 3488 and the amount of undetected photons due to dead time is 7196.

Appendix C – Dead Time Induced Image Inversion

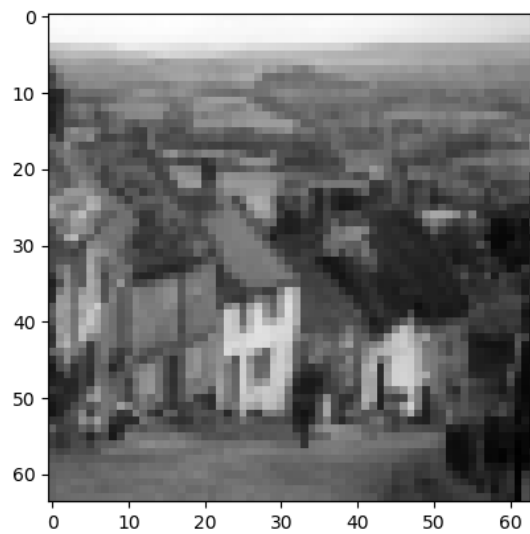


FIGURE 29: Original target image with the resolution of 64x64.

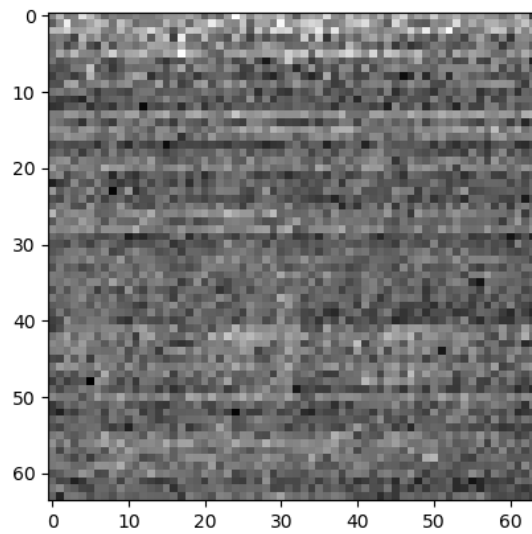


FIGURE 30: Photon rate = 100 (photons/pattern duration), pattern duration = 1 ms.

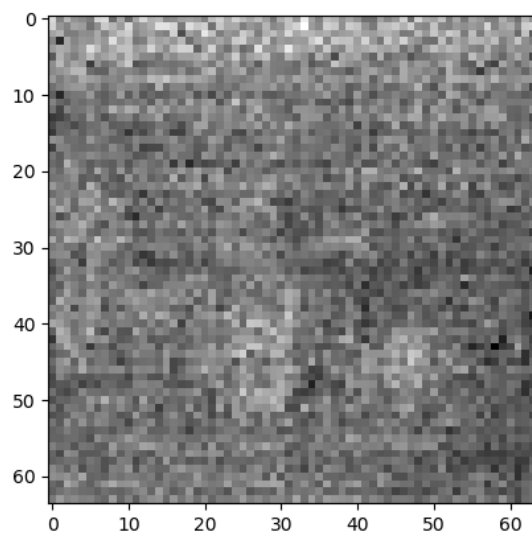


FIGURE 31: Photon rate = 500 (photons/pattern duration), pattern duration = 1 ms.

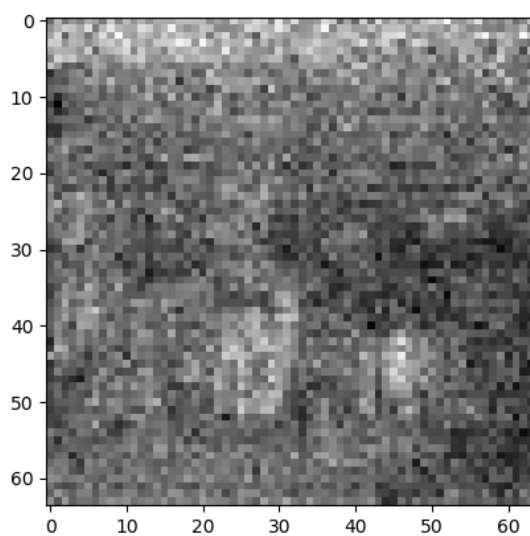


FIGURE 32: Photon rate = 1000 (photons/pattern duration), pattern duration = 1 ms.

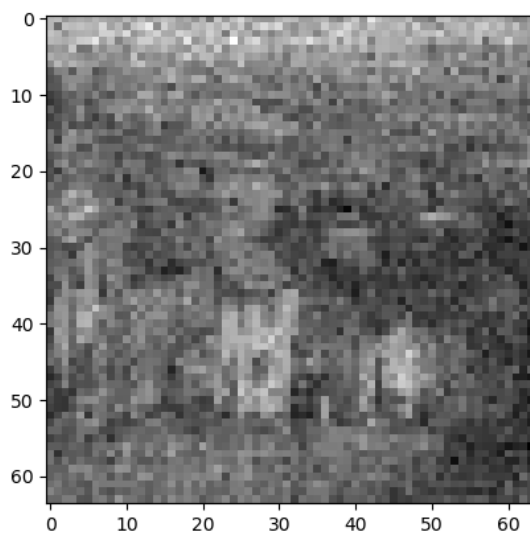


FIGURE 33: Photon rate = 2500 (photons/pattern duration), pattern duration = 1 ms.

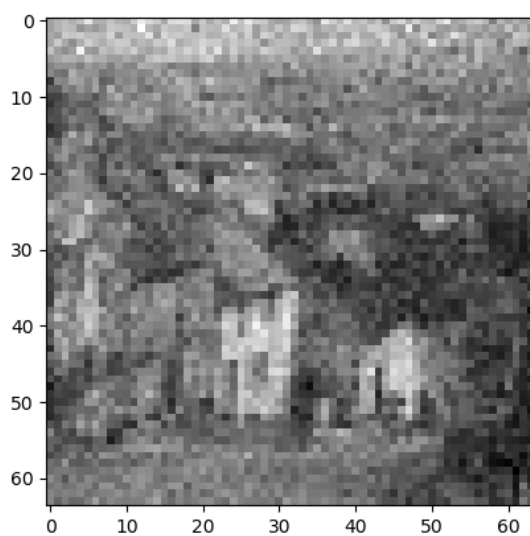


FIGURE 34: Photon rate = 5000 (photons/pattern duration), pattern duration = 1 ms.

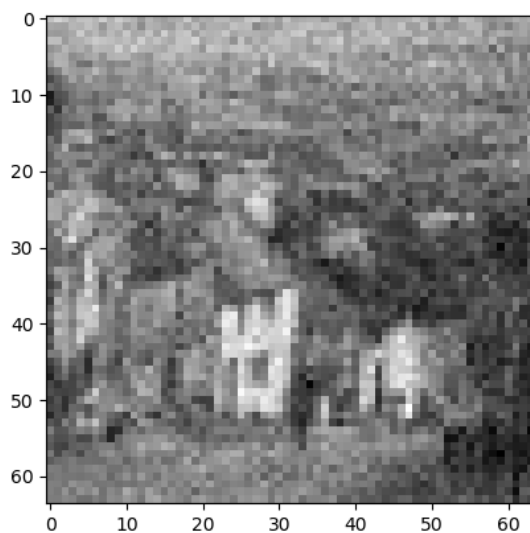


FIGURE 35: Photon rate = 7500 (photons/pattern duration), pattern duration = 1 ms.

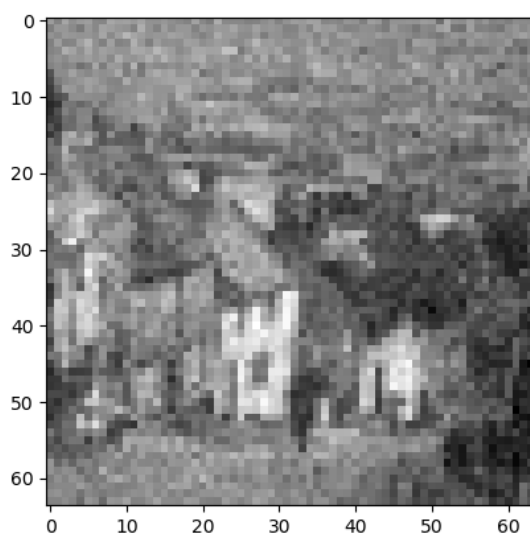


FIGURE 36: Photon rate = 12500 (photons/pattern duration), pattern duration = 1 ms.

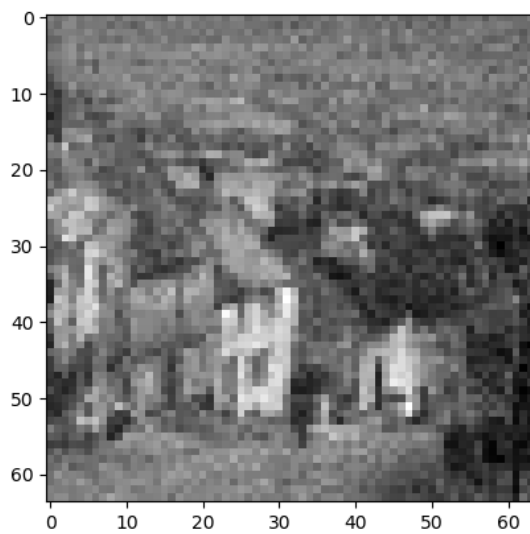


FIGURE 37: Photon rate = 15000 (photons/pattern duration), pattern duration = 1 ms.

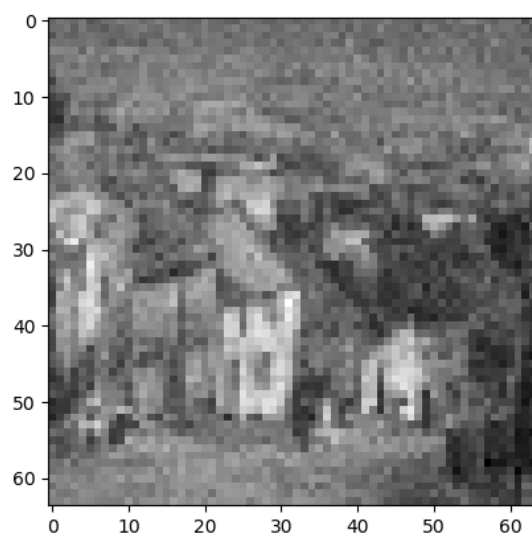


FIGURE 38: Photon rate = 17500 (photons/pattern duration), pattern duration = 1 ms.

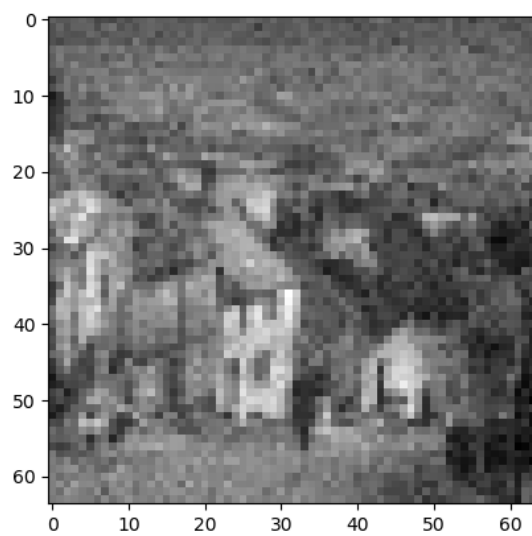


FIGURE 39: Photon rate = 20000 (photons/pattern duration), pattern duration = 1 ms.

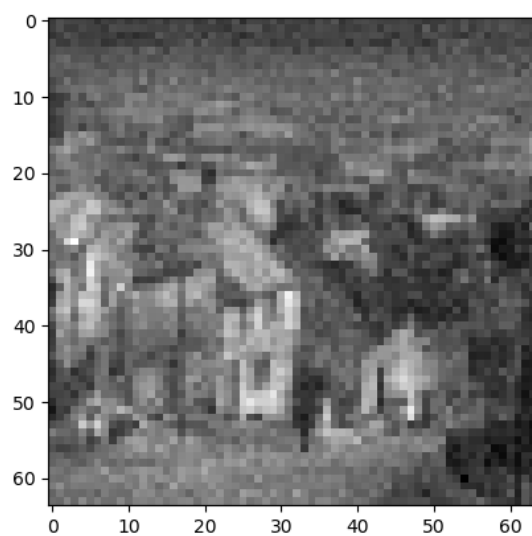


FIGURE 40: Photon rate = 25000 (photons/pattern duration), pattern duration = 1 ms.

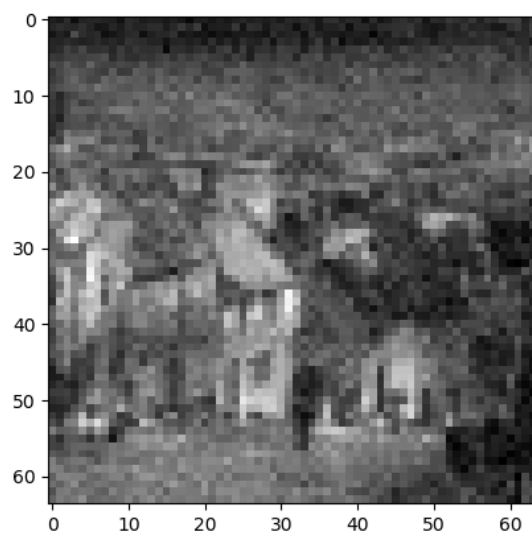


FIGURE 41: Photon rate = 30000 (photons/pattern duration), pattern duration = 1 ms.

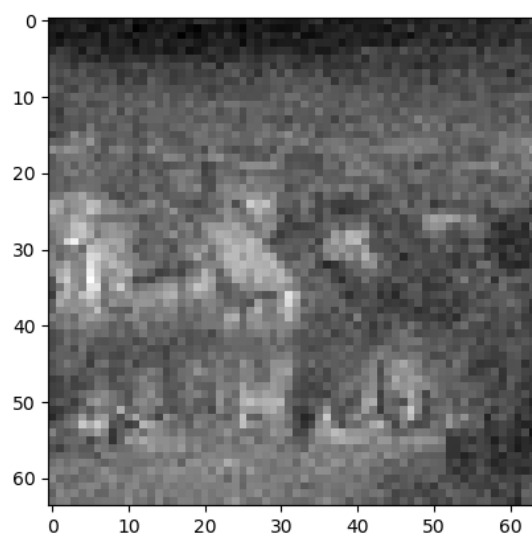


FIGURE 42: Photon rate = 40000 (photons/pattern duration), pattern duration = 1 ms.

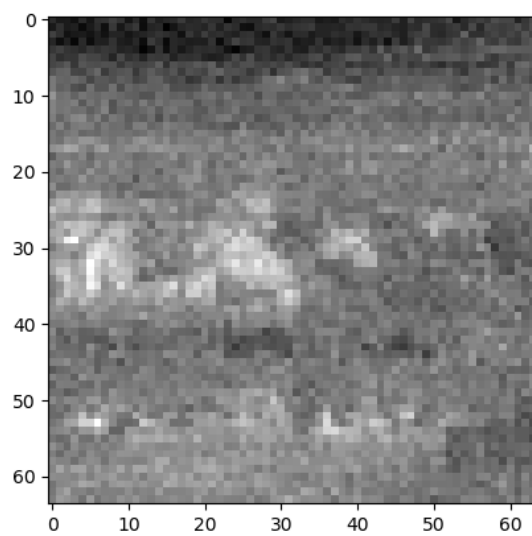


FIGURE 43: Photon rate = 50000 (photons/pattern duration), pattern duration = 1 ms.

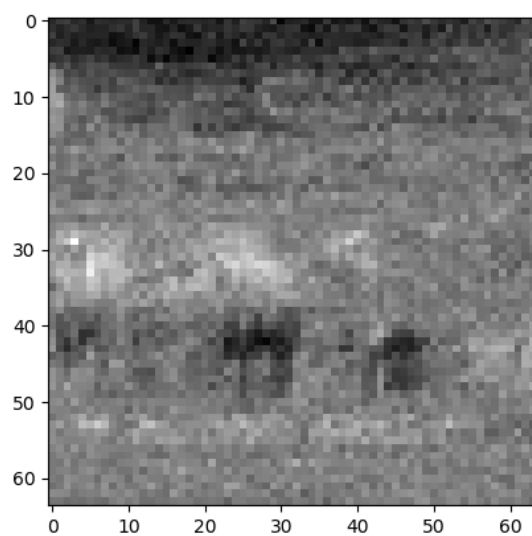


FIGURE 44: Photon rate = 60000 (photons/pattern duration), pattern duration = 1 ms.

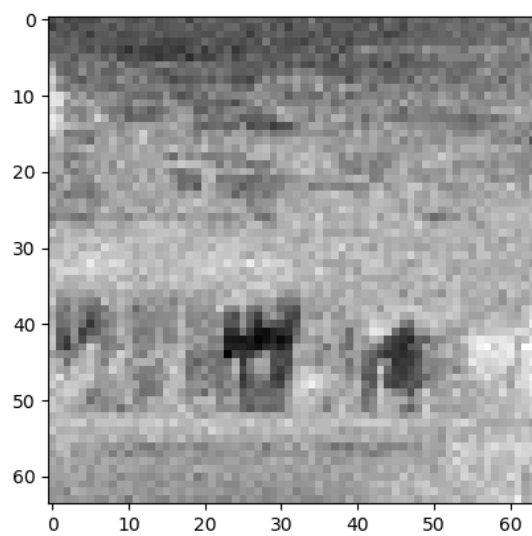


FIGURE 45: Photon rate = 70000 (photons/pattern duration), pattern duration = 1 ms.

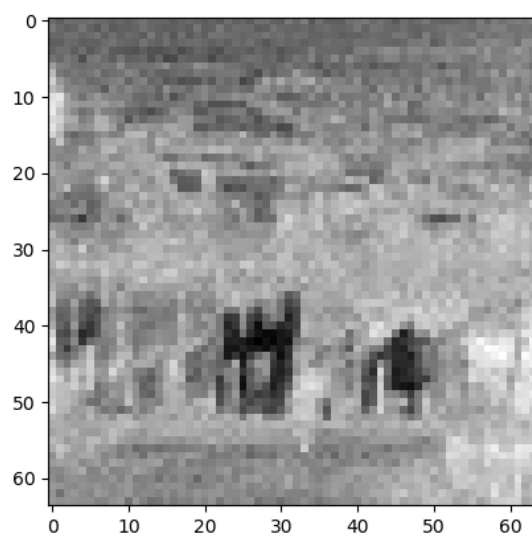


FIGURE 46: Photon rate = 80000 (photons/pattern duration), pattern duration = 1 ms.

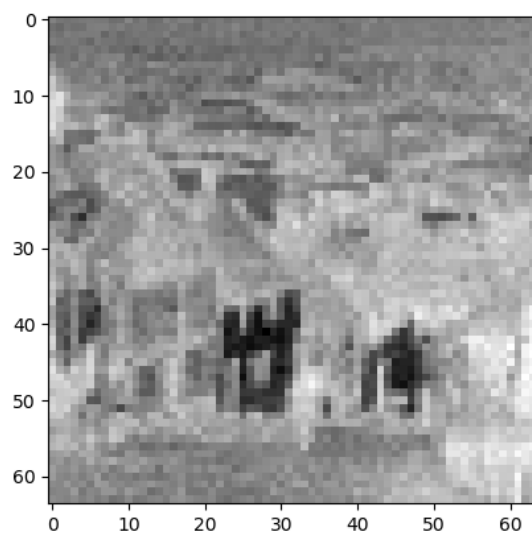


FIGURE 47: Photon rate = 90000 (photons/pattern duration), pattern duration = 1 ms.

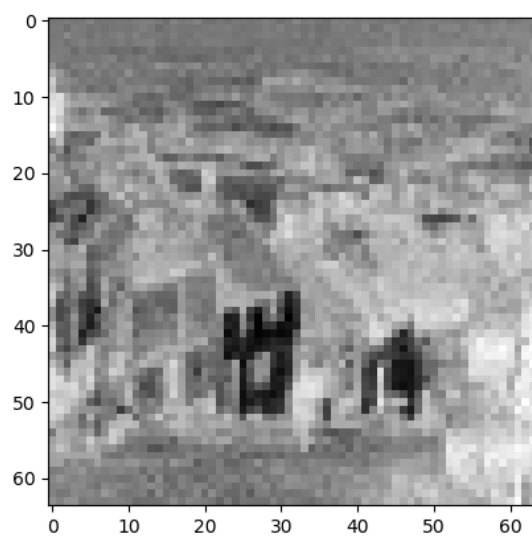


FIGURE 48: Photon rate = 100000 (photons/pattern duration), pattern duration = 1 ms.

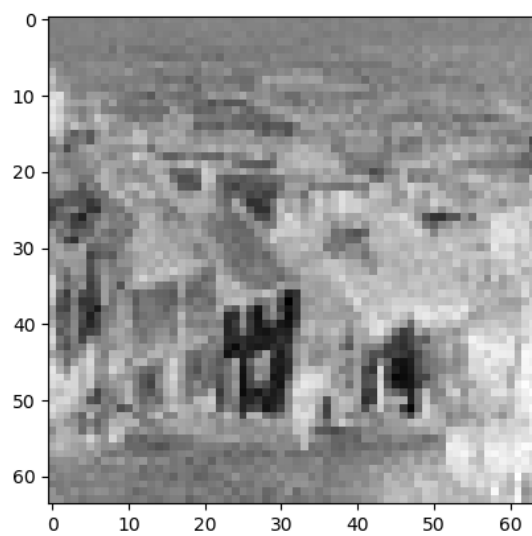


FIGURE 49: Photon rate = 110000 (photons/pattern duration), pattern duration = 1 ms.

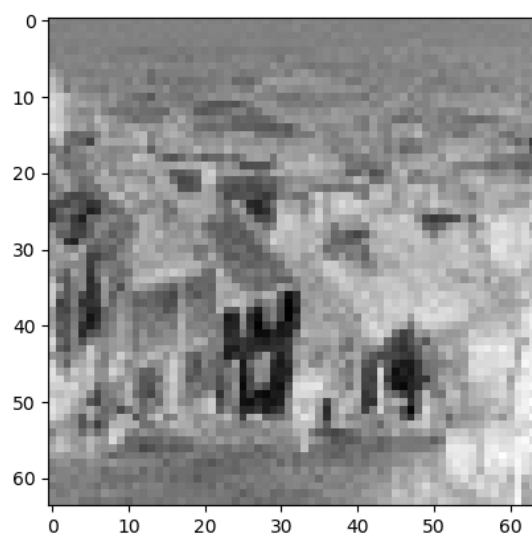


FIGURE 50: Photon rate = 120000 (photons/pattern duration), pattern duration = 1 ms.

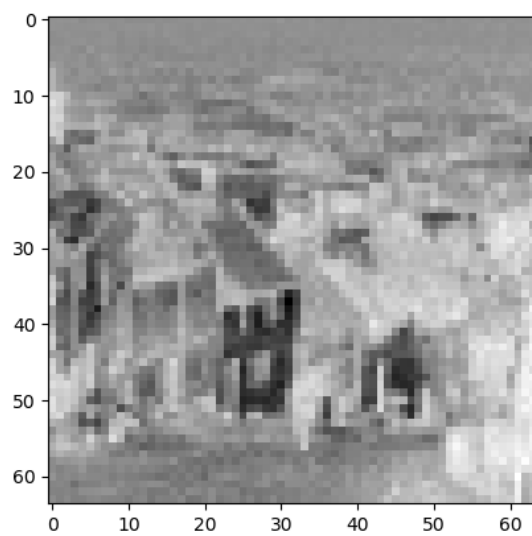


FIGURE 51: Photon rate = 130000 (photons/pattern duration), pattern duration = 1 ms.

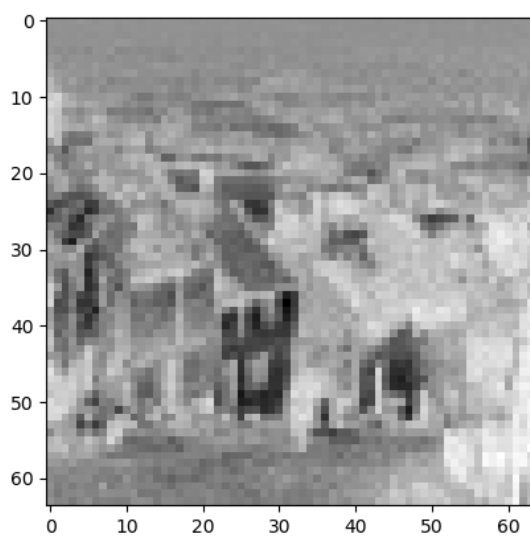


FIGURE 52: Photon rate = 140000 (photons/pattern duration), pattern duration = 1 ms.

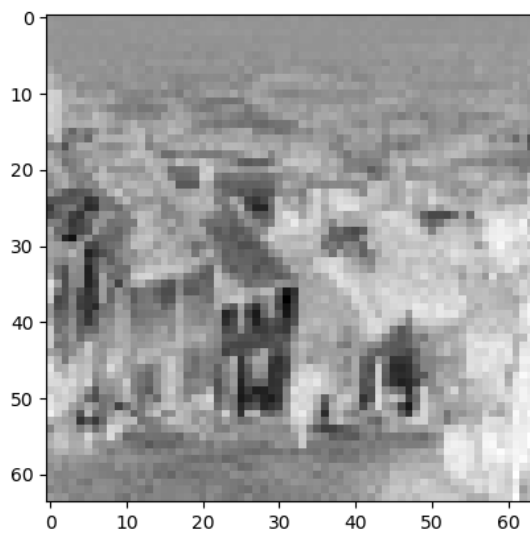


FIGURE 53: Photon rate = 150000 (photons/pattern duration), pattern duration = 1 ms.

Non-exclusive licence to reproduce thesis and make thesis public

I, Jan Bogdanov,

1. herewith grant the University of Tartu a free permit (non-exclusive licence) to reproduce, for the purpose of preservation, including for adding to the DSpace digital archives until the expiry of the term of copyright, **Experiment Design for a 3D Ghost Imaging Setup Utilizing a LinoSPAD Sensor**, supervised by Andreas Valdmann.
2. I grant the University of Tartu a permit to make the work specified in p. 1 available to the public via the web environment of the University of Tartu, including via the DSpace digital archives, under the Creative Commons licence CC BY NC ND 3.0, which allows, by giving appropriate credit to the author, to reproduce, distribute the work and communicate it to the public, and prohibits the creation of derivative works and any commercial use of the work until the expiry of the term of copyright.
3. I am aware of the fact that the author retains the rights specified in p. 1 and 2.
4. I certify that granting the non-exclusive licence does not infringe other persons' intellectual property rights or rights arising from the personal data protection legislation.

Jan Bogdanov
13/05/2019